J. Mech. Phys. Solids 195 (2025) 105924

Contents lists available at ScienceDirect

Journal of the Mechanics and Physics of Solids

journal homepage: www.elsevier.com/locate/jmps

On the effect of nuclear fission cladding stresses on Zirconium hydride orientation and dislocation strain energy fields via discrete dislocation plasticity and crystal plasticity finite element modelling

Christos Skamniotis [a,*], Daniel Long [b], Mark Wenman [b], Daniel S. Balint [c]

[a] Department of Engineering, King's College London, Strand Campus, WC2R 2LS, United Kingdom
[b] Department of Materials & Centre for Nuclear Engineering, Imperial College London Exhibition Road, London SW7 2AZ, United Kingdom
[c] Department of Mechanical Engineering, Imperial College London, UK

ARTICLE INFO

Keywords:
Discrete dislocation plasticity
Crystal plasticity finite elements
Delayed hydride cracking
Strain energy
Zirconium hydrides
Residual hydrostatic stresses

ABSTRACT

The diffusion of hydrogen in Zircalloy fuel cladding components and its associated delayed hydride cracking (DHC) mechanism remain a bottleneck in nuclear fission. Through Crystal Plasticity Finite Element (CPFE) analysis at the grain scale (μm) and Discrete Dislocation Plasticity (DDP) at the hydride scale (nm), we explore how cladding stress history influences the dislocation network in a system of hydrides, and in turn, how this can impact hydrogen accumulation and embrittlement. CPFE indicates that high tensile stresses at service temperature can cause severe plasticity at a notch of a cladding component, leading to significant residual compressive stresses on service shutdown. As a result, hydrides evolve in this service scenario under a cyclic tensile-compressive background stress, which is found to enhance the ratchetting of dislocations compared to a typical constant background stress history and to eliminate the concentration of tensile residual hydrostatic stresses at the locations of dissolved hydrides. Since these tensile residual stresses drive the local accumulation of hydrogen during progressive precipitation-dissolution cycles, a key question is posed as to whether and how the sequencing of cladding stress-temperature reversals influences the growth rate of macro-hydride colonies. Simultaneously, we find that a large fraction of the total strain energy of hydrides is associated with the strain energy of dislocations and their interactions, posing the question of whether dislocation networks influence the energetically favourable hydride orientation. Our study provides a foundation for future studies of the DHC mechanism and drives the development of thermodynamically consistent dislocation-based models coupled with irradiation effects.

1. Introduction

Hydrogen uptake in nuclear reactor components continues to pose major scientific and technological challenges that hinder our transition to net zero. A major problem is the embrittlement and fracture of Zirconium based fuel cladding components via the Delayed Hydride Cracking (DHC) mechanism, underpinned by the diffusion of hydrogen atoms and their subsequent precipitation into

* Corresponding author.
E-mail address: christos.skamniotis@kcl.ac.uk (C. Skamniotis).

https://doi.org/10.1016/j.jmps.2024.105924
Received 25 April 2024; Received in revised form 15 October 2024; Accepted 28 October 2024
Available online 2 November 2024

Zirconium hydrides (Motta et al., 2019). An obstacle to understanding and mitigating DHC is the complexity of the underlying physics involved, associated with the crystallography of the Zirconium matrix and Zirconium hydrides, the hydrogen precipitation and dissolution kinetics, the cladding texture, as well as the thermomechanical loading cycles encountered during nuclear fission. The reader is referred to Patel et al. (2021); Liu et al. (2021) for a detailed description of these above aspects and particularly hydrogen diffusion at notches and defects of Zirconium-based components (Liu et al., 2021).

Experiments and modelling have established that each cooling cycle favours the sympathetic nucleation and growth of hydride platelets or needles (length <1 μm), in the form of inter-linked hydride stringers spanning hundreds of μm in length (macro-hydrides) (Cinbiz et al., 2016). One of the remaining challenges is to understand and prevent the formation of hydride stringers along the radial direction of the cladding tube, which assist cracks to propagate quickly through the tube thickness (Sunil et al., 2020; Vizcaino et al., 2014; Chu et al., 2008; Cui et al., 2009; Colas et al., 2014). Strong experimental evidence shows that these radial stringers develop via the so-called 'hydride re-orientation effect' activated by the hoop tensile stresses in the tube associated with internal fuel pressure (Cinbiz et al., 2016; Khan et al., 2021; Simon et al., 2021). However, most of the knowledge in this aspect remains phenomenological.

Computational modelling allows for a mechanistic understanding of the re-orientation effect, particularly in situations where experimental observations are hindered by the short time scales and length scales of hydride phase transformations (Bair et al., 2017). Phase Field models have contributed the most to this area (Simon et al., 2021; Shi and Xiao, 2015; Xiao et al., 2015) and demonstrated through energetic principles that in the absence of tensile hoop stress the hydride stringers grow circumferentially (hoop direction), but when a tensile hoop stress beyond a certain threshold is applied, the stringers re-orient radially. Recently, it has become clear that the crystallographic relation $\{0001\}_{Zr}//\{111\}_{ZrH}$ and $\langle 1120\rangle_{Zr}//\{110\}_{ZrH}$ (assuming stable δ phase $ZrH_{1.5–1.7}$) between the Zr matrix and each individual hydride of the stringer remains unchanged, which implies that re-oriented stringers consist of hydrides stacked in parallel basal planes (c axis of Zr is aligned radially) (Motta et al., 2019; Bair et al., 2015). This feature has been hardly evidenced through microscopy.

Phase Field approaches have shown low merit in tackling the computational challenge of capturing the large length scale difference between individual hydrides within a grain and hydride stringers spanning multiple grains (Motta et al., 2019; Patel et al., 2021). This milestone is necessary to understand and potentially mitigate DHC failure through optimising alloy microstructure and/or reactor operation conditions (Tondro et al., 2022). Furthermore, Phase Field models disregard the statistical and discrete nature of localised plastic deformation encountered during a hydride precipitation-dissolution cycle (Tummala et al., 2018; Skamniotis et al., 2024). This concerns dislocation nucleation and glide along the discrete slip systems consistent with the crystallography of matrix and hydride phases, not to mention their interaction with prismatic dislocation loops and defect clusters associated with irradiation creep effects.

Recently, the authors showed that discrete dislocation plasticity (DDP) models can explicitly capture the above phenomena and can also communicate with continuum scale Crystal Plasticity Finite Element (CPFE) models (Skamniotis et al., 2024) and/or recently developed pseudo-analytical reduced order schemes (Patel et al., 2021), towards addressing the pressing need for multi-scale models of DHC failure. Our recent DDP studies quantified the degree by which hydride misfit stresses can be relaxed by plastic deformation, subject to crystallographic limitations, i.e. availability of slip systems (Skamniotis et al., 2024; Reali et al., 2022a). Our latest study (Skamniotis et al., 2024) placed special attention to the interaction of misfit stresses with the background stress field generated at a notch of Zirconium cladding components as well as to the effect of grain size on the relaxation of misfit stresses; it also showed that microstructural obstacles can enhance the irreversibility of plastic deformation (slip), by preventing dislocations to glide backwards when the misfit stresses are removed during hydride dissolution. Since the remaining dislocation structure is known to control the residual hydrostatic stresses that drive hydrogen accumulation at locations of previously precipitated hydrides ('memory effect') (Patel et al., 2021; Reali et al., 2021a; Reali et al., 2022b), we can argue that an explicit modelling of dislocation interactions through DDP-type analysis is essential in predicting hydride stringer growth, re-orientation, and interlinking. The contributions of the present study are targeted at this research direction.

While our latest study (Skamniotis et al., 2024) only looked at stresses encountered during precipitation-dissolution cycles of a single isolated δ hydride, under a constant tensile background stress at a particular orientation with the respect to the hydride, the present study will additionally consider:

1) both the metastable γ-ZrH hydride and stable δ hydride phase, including the first ever explicit modelling of phase transition from γ to δ during cooling,
2) a cyclic background stress field which does not vary in phase with the hydride precipitation-dissolution cycles and takes into account, for the first time, the compressive residual stresses that can be practically encountered on reactor shut-down, obtained by hand-in-hand cyclic CPFE analysis at the grain-scale,
3) the evolution of dislocation structure and associated fields that control hydrogen trapping/accumulation encountered during the progressive growth of a hydride stringer consisted of five individual hydrides under different background stress cycling conditions,
4) the first ever analysis of individual strain energy components underpinning the interaction between hydrides, dislocations and background stress, to unravel previously unexplored hydride orientation effects and to identify minimum energy configurations.

It should be emphasised that despite the wealth of literature in the field, the concept of configurational energy of dislocations and the aspect of compressive residual stresses have not been considered in the context of DHC failure so far. Our findings surrounding these two aspects will support that future studies surrounding the energetics of hydride growth and the associated reduction of Gibb's free energy should take into account the discrete nature of plasticity and the irreversibility effects of dislocation structure evolution. Our present study lays the foundation for incorporating these aspects in such future studies.

Additionally, our newly proposed strain energy interaction analysis provides a steppingstone to incorporating irradiation effects in

the understanding of the DHC process through further advancement of the DDP framework developed here, e.g., by adding the prismatic dislocation loops that are physically induced by neutron bombardment of the microstructure. It also serves the development of thermodynamically consistent DDP-based models of hydride stringer growth since it can be readily coupled with explicit calculations of phase energy and hydrogen diffusion. Although we consider a 2D simulation plane here, such a simplification is instructive to simultaneously aid the future development of 3D Discrete Dislocation Dynamics models (Tummala et al., 2018) coupled with strain energy calculations, while retaining the salient features of a very complex DHC problem, including microstructure fidelity, discrete crystallographic representations of dislocation plasticity and hydrides, electronic structure informed stress-driven diffusion of hydrogen, thermodynamically consistent precipitation kinetics, stress states of notch flaws and thermomechanical cycling of practical relevance to reactor service scenarios. Combined, the above work packages may eventually enable the accurate prediction and mechanistic understanding of the detrimental hydride stringer re-orientation effect in full three-dimensional space.

2. CPFE analysis of grain-scale stresses

2.1. CPFE methodology

We consider the notched three-point bending model in Fig. 1a with the aim to capture qualitatively the stress state conditions encountered at the notch of a Zircalloy (Zr-4) cladding component during cyclic thermomechanical loading. The cladding texture of interest here is the one with the c-axis along the radial tube direction, which maximises resistance to DHC failure (Murty and Charit, 2006); this radial direction coincides with the direction of the dashed line A-A′ denoted in Fig. 1a, such that the c-axis of all the

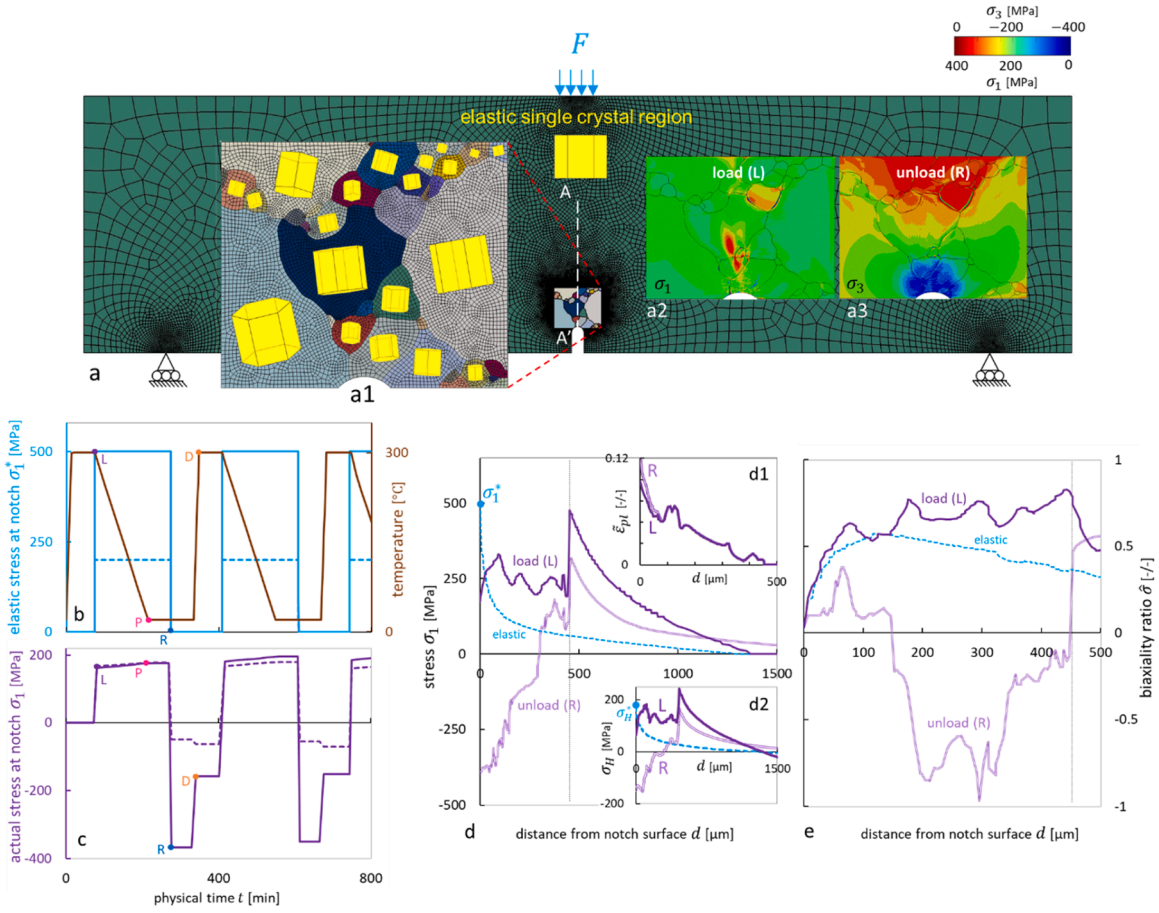

Fig. 1. Summary of CPFE analysis. a) Three-point bending model of Zr-4 alloy (adapted from Long et al. (2023)); a1) polycrystalline microstructure at the notch region (EBSD data from Wan (2020)); a2) maximum principal stress σ_1 field at the notch region at load (instance L) and a3) residual minimum principal stress σ_3 field at the notch region at unload (instance R). b) Applied histories of elastic stress at notch surface σ_1^* and temperature T; c) corresponding history of actual stress at notch surface. d) σ_1 variation along the A′-A path at instances L (load) and R (unload/residual); d1-d2) corresponding effective plastic strain $\bar{\varepsilon}_{pl}$ and hydrostatic stress σ_H distributions. e) Corresponding stress biaxiality ratio $\hat{\sigma}$ variation along A′-A. In Fig. 1b-c, the dashed trace represents the elastic shakedown case with $\sigma_1^* = 200$ MPa at load, whereas the bold trace represents plastic shakedown with $\sigma_1^* = 500$ MPa at load.

microstructural grains in Fig. 1a1 also approximately align with A-A′; this implies that the maximum principal stress encountered at the vicinity of the notch during loading approximately applies along the isotropic basal plane. We assume that plasticity is localised at the notch region and the remaining volume behaves elastically. The latter is therefore prescribed to obey an elastic single crystal response whereas the notch region is described in detail as a blocky-alpha microstructure (see Fig. 1a1) and obeys the slip rule (Dunne et al., 2007):

$$\dot{\gamma}^i = \rho_m \nu_D b^2 \exp\left(\frac{-\Delta F}{kT}\right) \sinh\left(\frac{(\tau^i - \tau_c^i)\Delta V}{kT}\right) \tag{1}$$

where $\dot{\gamma}^i$ is the slip rate in ith slip system, T is the temperature, $\tau^i - \tau_c^i$ is the difference between the applied resolved shear stress and the temperature dependent critical resolved shear stress τ_c^i, ρ_m is the mobile dislocation density, ν_D is the Debye frequency of atomic vibrations, b is the Burgers vector magnitude, ΔF is the activation energy for dislocation glide and ΔV is the activation volume (Zheng et al., 2016a). Values are given in Table 1. Details of the CPFE analysis are given in (Long et al., 2023) and Appendix A.

The bending load F is chosen such that a target value of 'elastic' maximum principal stress σ_1^* would occur at the notch vicinity/surface if the notch region also behaved elastically; we refer to this here as 'elastic stress at notch' σ_1^* (Skamniotis and Cocks, 2022a). This stress is prescribed to vary out-of-phase with temperature T as shown in Fig. 1b, which reflects in-service thermomechanical load characteristics (Motta et al., 2019; Liu et al., 2021). We apply a low amplitude $\sigma_1^* = 200$ MPa and a high amplitude $\sigma_1^* = 500$ MPa, which respectively lead to elastic and plastic shakedown states at the notch vicinity, as explained below. The temperature dependent prismatic slip strength $\tau_c(T)$ of Zr-4 (Liu et al., 2021; Gong et al., 2015) implies $\tau_c(20^\circ) = 152$ MPa and $\tau_c(300^\circ) = 65$ MPa at the lower and higher temperature extremes of the cycle, which correspond to yield stresses in the ranges $\sigma_y(20^\circ) = 304$–350 MPa and $\sigma_y(300^\circ) = 130$–$150$ MPa arising from the Schmid factor range $M = 0.433$–0.5 specific to uniaxial loading in the basal plane of the grain at the notch vicinity of Fig. 1a1. In fact, this grain is oriented here such that $M \sim 0.45$ in the most active slip system, leading to a yield stress range $\sigma_y(20^\circ) + \sigma_y(300^\circ) = 482$ MPa between the two extremes of the cycle—this range cannot accommodate the elastic stress amplitude $\sigma_1^* = 500$ MPa. Thus, in this case the residual stresses generated on unloading are expected to exceed yield such that cyclic plastic deformation occurs and continues to occur with further cycling, i.e. plastic shakedown prevails (Skamniotis and Cocks, 2022a); whereas, the amplitude $\sigma_1^* = 200$ MPa can be well contained within the above yield range and therefore plasticity is expected to occur only during the loading phase of the first cycle, i.e. elastic shakedown prevails (Skamniotis and Cocks, 2022b).

2.2. CPFE results

Fig. 1c shows the actual stress histories σ_1 at the notch surface corresponding to the applied elastic stress σ_1^*—temperature T histories in Fig. 1b. The amplitudes $\sigma_1^* = 200$ MPa and $\sigma_1^* = 500$ MPa lead to very similar actual stresses $\sigma_1 \sim 150$ MPa on loading (instance L—Fig. 1b and c), since these are limited by the high temperature yield strength, whereas the residual stresses on unloading

Table 1
Material properties and DDP parameters used in the study, unless otherwise specified.

Material properties		
Burger's vector magnitude	*B*	0.32 [nm]
shear modulus	*μ*	33 [GPa]
Poisson's ratio	*ν*	0.34
critical resolved shear stress (CRSS) for prismatic slip	τc	26.3 exp(514.7/*T*) [MPa]
activation energy	*Δf*	0.32 eV
activation volume	*ΔV*	20.93 b3
mobile dislocation density	*ρm*	0.01 [μm^{-2}]
frequency of atomic vibrations	*νD*	1011 [Hz]
Boltzmann constant	*K*	1.38×10^{-23} [J K^{-1}]
drag coefficient	*B*	5×10^{-5} [Pa s]
source nucleation time	*ts*	1 [ns]
source strength = CRSS	*τs*	26.3 exp(514.7/*T*) [MPa]
source strength (CRSS) at room temperature	*τS0*	152 [MPa]
source nucleation length	*LS*	μb/2πτ (1-ν) [nm]
obstacle strength	*τobs*	3τs0 [MPa]
source density	*ρs*	30 [μm^{-2}]
obstacle density	*ρobs*	150 [μm^{-2}]
DDP parameters		
grain size	*Lg*	10 [μm]
source-obstacle (s-o) box size	*Ls-o*	5 [μm]
integration element size	–	0.01 [μm]
time increment	*dt*	10 [ps]
max allowable dislocation velocity		200 m/s
dislocation annihilation distance	–	8*b*
min source-source spacing (in multiples of *LS*)	–	1
min source-obstacle spacing (in multiples of *LS*)	–	1/3
slip plane spacing	–	*lSP=120b*

(instance R—Fig. 1b and c) differ significantly and are consistent with our expectations of elastic and plastic shakedown: $\sigma_1^* = 200$ MPa results in very low residual values $\sigma_1 \sim -50$ MPa (dashed line) whereas $\sigma_1^* = 500$ MPa leads to $\sigma_1 \sim -350$ MPa which satisfies yield at room temperature; once re-heating to 300 °C occurs (instance D—Fig. 1bc) the latter reduces to $\sigma_1 \sim -150$ MPa since it becomes limited by the high temperature yield stress. Evidence of plasticity on unloading (R) for the case $\sigma_1^* = 500$ MPa is given by the inset Fig. 1d1 where the effective plastic strain $\widetilde{\varepsilon}_{pl}$ distribution along the A-A′ path ahead of the notch is shown to enhance from instance L to R. The corresponding changes in maximum principal stress distribution between instances L and R are shown in Fig. 1d, highlighting the severity of compressive residual stresses near the notch at R. The result for the case $\sigma_1^* = 200$ MPa is not shown as this would only give zero residual stresses except for small values heavily localised to the notch vicinity ($d < 20$ μm).

The immediate increase of σ_1 as one departs from the notch vicinity ($d = 0$ μm) at the load instance L in Fig. 1d is explained by the associated increase of the stress biaxiality $\widehat{\sigma} = \sigma_2/\sigma_1$ in Fig. 1e (σ_2 = medium principal stress—note: plane stress conditions are assumed here). While this increase associates with a rise in the hydrostatic stresses $\sigma_H = \sigma_1 + \sigma_2$ plotted in Fig. 1d2 (2D plane stress conditions), it does not imply increase in deviatoric stresses which drive plasticity. Upon unloading (instance R—Fig. 1e), the distribution of stress biaxiality, defined here as $\widehat{\sigma} = \sigma_2/\sigma_3$, changes rapidly and leads to negative values at distances $150 < d < 450$ μm from the notch vicinity, implying that compressive and tensile principal stresses apply simultaneously in this region.

3. Link between grain-scale and hydride-scale stresses

The key indication of our CPFE analysis of grain-scale stresses in Section 2.2 is that severe in-service mechanical loads at high

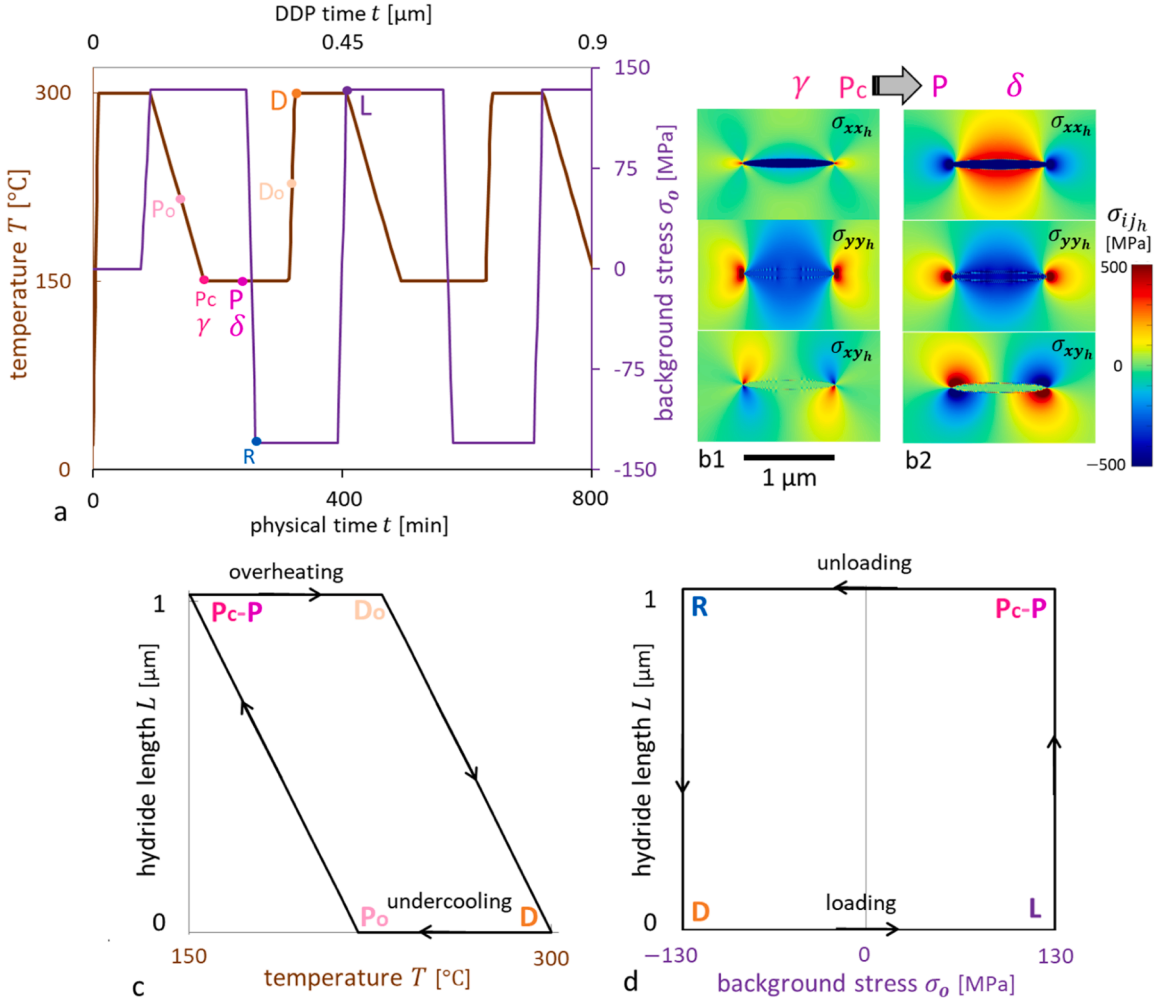

Fig. 2. Key features of DDP analysis. a) Thermomechanical load history in real/physical time and scaled/DDP time, showing the out-of-phase cyclic variation of temperature T and background stress σ_0. b1) Hydride 'misfit' stress field components σ_{ij_h} in the basal HCP plane induced by the anisotropic transformation strain of γ-hydride; b2) corresponding stress fields induced by the isotropic transformation strain of δ-hydride. c) Hydride length L—temperature T cycle highlighting the amount of undercooling and overheating used (Passelaigue et al., 2021). d) Hydride length L—background stress σ_o cycle highlighting the four key instances in the cycle where plasticity occurs.

temperature (i.e. severe elastic stresses σ_1^*) can lead to significant compressive residual stresses on unloading, i.e. during service shutdown, and that this largely owes to the reduction of slip strength of Zr-4 at high temperature compared to room temperature. We will utilise this information here to investigate the effect of the cyclic stress—temperature history at the grain/CPFE length-scale on the cyclic stresses and dislocation structures that occur in the hydride/DDP length-scale. This will be achieved by the DDP analysis framework given in Fig. 2. The type of analysis here allows us to assume that the growth of a single hydride at the notch vicinity occurs in a length-scale small enough (<1 μm) such that grain-scale stresses can be considered uniform. Hence, in what follows, we deploy DDP models in which hydrides precipitate/dissolve under a uniform 'background stress' field σ_{oij}, relevant to the local σ_1 stress history evaluated through CPFE analysis.

Although the CPFE results in Fig. 1d and e provide a variety of multiaxial stress states to use as σ_{oij} in DDP analysis, we will only consider here the uniaxial state at the notch vicinity. This is because our study here does not explicitly account for the evolution of hydrogen concentration in the notch region, which is largely controlled by the hydrostatic stress field and hence the details of stress multiaxiality. Rather, it focuses on the evolution of dislocation structure during hydride growth/dissolution, which is sensitive to the deviatoric stress field ahead of the notch. Hence, we only need to consider here the deviatoric part of a 'background stress' stress state in DDP analysis, which is simply achieved by applying a uniaxial σ_{oij} state of magnitude σ_o.

Fig. 2a shows the cyclic background stress—temperature $\sigma_o - T$ history prescribed in our DDP analysis. Although this history could have been made identical to the $\sigma_1 - T$ history in Fig. 1b and c, we prefer here to simplify the variation of $\sigma_o - T$ in order to aid a mechanistic and systematic understanding of σ_o cycling effects. In particular, the simplified history in Fig. 2a allows us to systematically explore the isolated effect of σ_o history whilst keeping the temperature T and hydride length L histories the same, i.e. T variation between 150 °C and 300 °C and L variation between 0 and 1 μm (see Fig. 2c). Building on the above assumption, we consider three σ_o histories:

A). cyclic stress σ_o between 130 MPa at instance L and $-$ 130 MPa at instance R (plotted in Fig. 2a).
B). non-cyclic/constant stress $\sigma_o = 130$ MPa,
C). zero stress $\sigma_o = 0$ MPa.

We argue here that if the DDP analysis were to use the exact σ_1 histories obtained from CPFE analysis (Fig. 1b and c), then additional considerations would be necessary. For example, if cooling was performed down to 20 °C instead of the 150 °C in Fig. 2a, then the slip strength of Zr-4 at full hydride precipitation P would increase by a factor of 1.7, implying significantly lower slip activity; on the other hand, cooling at 20 °C in reality exerts a much higher driving force for precipitation, promoting larger hydride sizes and potentially more severe slip activity. This competition arising from the interplay between plasticity and the thermodynamics of phase transformation (Khan et al., 2021; Gill et al., 2001) cannot be explored here since our $T-L$ cycles are currently predefined. Furthermore, we do not explicitly account for the evolution of hydrogen concentration, both at the grain length-scale and the hydride length-scale. These support further our current strategy of keeping the $T-L$ cycles consistent and simple enough in order to unravel the isolated effect of σ_o cycling on the evolution of the dislocation network. In this regard, our main concern here is the amplitude of background stress σ_o, which is conservatively chosen as 130 MPa to ensure that plasticity at the DDP-scale does not occur in the matrix alone, i.e. without adding the hydride misfit/transformation stresses. This is consistent with the CPFE results in Fig. 1c which indicate that the grain-scale stress at the notch vicinity cannot exceed yield. Further justification on the chosen magnitude of σ_o for DDP analysis is given by the authors in (Skamniotis et al., 2024).

4. DDP analysis of single hydride

4.1. DDP methodology

A detailed description of the DDP formulation is given in Reali et al. (2022a) and Balint et al. (2006). Here will only provide details related to the implementation of DDP on the problem of Zirconium hydrides.

Our DDP model uses the prescribed hydride length L, temperature T and background stress σ_o histories associated with the $L-\sigma_o$ and $L-\sigma_o$ cycles in Fig. 2c and d, including the following sequence of events/instances: hydride nucleation (Po), completion of γ hydride precipitation (Pc), completion of conversion to δ hydride (P), completion of unloading to a residual state (R), onset of dissolution (Do), completion of dissolution (D), and completion of re-loading (L). The hysteresis cycle in Fig. 2c implies that an undercooling and overheating of 80 °C are required for nucleation (Po) and the onset of dissolution (Do), respectively (Liu et al., 2021; Passelaigue et al., 2021). For the purposes of the present work, we will adopt the simplification used in our earlier studies (Skamniotis et al., 2024; Reali et al., 2022a) in that the hydride precipitation-dissolution cycles are slow enough such that any transient hydrogen diffusion processes can be ignored for studying dislocation-based mechanisms, i.e., we can assume that the local hydrogen concentration field is always at steady-state/equilibrium. We also treat the hydrides as homogeneous inclusions, i.e. same elastic properties between hydride and matrix, for the type of problem analysed here, in consistency with previous study where this assumption was justified (Reali et al., 2022a); here the reader is referred to Appendix B for an even more detailed justification.

We consider elliptical hydrides as an approximation of the needle-shape, with maximum length $L_{\max} = 1$ μm and width $w_{\max} = 0.1$ μm (as in Reali et al, (2022b)). In this Section 3, we focus on the first precipitation of a single γ hydride which converts to δ after cooling (Pc to P in Fig. 2a). Fig. 2b1 and b2 show the enhancement of misfit stress fields σ_{ij_h} in the isotropic basal plane upon conversion from γ phase with transformation strains $\widehat{\varepsilon}_x = 0.6$ %, $\widehat{\varepsilon}_y = 5.6$ %, into δ phase with $\widehat{\varepsilon}_x = \widehat{\varepsilon}_y = 4.6$ % (Carpenter, 1973). For given hydride

dimensions L, w (here $w = 0.1L$), the σ_{ij_h} fields are numerically reproduced by superimposing the stress fields of N edge dislocations with Burger's vector $b_x = L\widehat{\varepsilon}_x/N$ placed along the elliptical hydride interface and equally spaced along x, together with another N dislocations with Burger's vector $b_y = w\widehat{\varepsilon}_y/N$ along the same interface, equally spaced along y.

These misfit/special purpose dislocations have their extra half plane inside the hydride; this is shown in Fig. 3a1 using $N = 20$ for illustration purposes; the actual DDP simulations use $N = 100$, i.e. two families of 100 dislocations (orientated along x and y axes). We note that the method of using misfit/special purpose dislocations to capture the misfit stress field of elliptical hydrides has been extensively verified in Skamniotis et al. (2024) and Gill et al. (2001). In particular, we have verified that a large enough number of $N = 100$ dislocations reproduces exactly Eshelby's solution for the stress field of a homogeneous elliptical inclusion with isotropic transformation strains $\widehat{\varepsilon}_x = \widehat{\varepsilon}_y = \widehat{\varepsilon}$ (δ phase) and gives the analytical hydrostatic stress $\sigma_H = 2\mu\widehat{\varepsilon}/(1-\nu) = -4600$ MPa uniformly inside the hydride and zero hydrostatic stress outside it. Additionally, we enforce the common practise where the theoretically infinite stress at the dislocation core (based on textbook expressions) is prevented by applying a local regularisation/smoothening of the stress field near the core, as detailed in Gill et al. (2001). This regularisation, together with the use of a large number of superimposed misfit dislocations, eliminate any undesirable local stress concentrations that may have otherwise occurred along the hydride-matrix interface, ensuring that the use of many discrete misfit dislocations leads to a smooth and realistic stress field that does not adversely affect the DDP simulations. We also note that the discontinuity of the stress field at the interface (sudden change from tension to compression) is a true physical effect and is responsible for the pile-up of dislocations at its vicinity (Skamniotis et al., 2024; Gill et al., 2001), i.e., the dislocations are naturally predicted to pile-up at the hydride-matrix interface under the influence of the misfit stress field alone and without needing to enforce a criterion for preventing dislocations to enter the hydride (or cut the interface); this adds merits to our overall DDP modelling technique. The reason for using misfit/special purpose dislocations to represent the misfit stress field is because this method offers versatility in capturing complex misfit stress fields that cannot be captured analytically, e.g. the stress field of the γ phase does not have a closed form solution; in addition, by changing the Burger's vector of misfit/special purpose dislocations one can switch from the misfit stress field of γ phase to the one corresponding to the δ phase.

Real crystallographic dislocations are generated by Frank-Read sources which together with obstacles are distributed randomly over a sufficiently large domain/box of 5 μm square side (Skamniotis et al., 2024), in which the hydride is centred. The misfit/special purpose interfacial dislocations used here to represent the misfit stress field of a coherent hydride do not interact with the real crystallographic dislocations generated by plasticity. However, implicit interaction occurs through their stress fields. Each edge dislocation dipole is nucleated as soon as its Frank-Read source experiences a resolved shear stress above the source strength, i.e. $\tau_i > \tau_s$ over a nucleation time $t_s = 1$ ns, where τ_s is taken equal to the temperature dependent critical resolved shear strength of Zr-4 for prismatic slip, i.e. $\tau_s = \tau_c(T)$.

The two-dimensional (2D) DDP simulation plane inherently poses the limitation/assumption that only prismatic slip occurs; this is

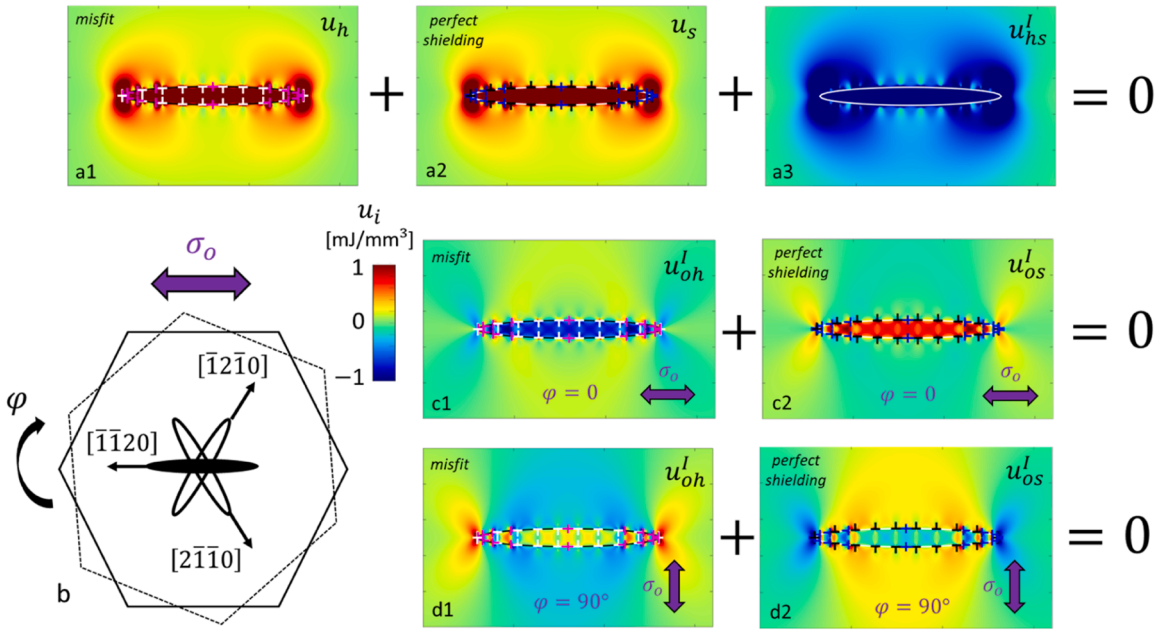

Fig. 3. Idealised paradigm: superpositions of strain energy density fields (J/m^3) associated with the strain energies in Eqs. (3a)–(3f), for the special case when the γ-hydride misfit stresses are 'perfectly' shielded/relaxed by edge dislocations located at the hydride-matrix interface. Horizontal and vertical dislocations with extra half planes inside the hydride produce the misfit stress field—corresponding dislocations with extra half planes outside the hydride impose the perfect shielding. a1–a3) Interaction between the hydride and the shielding dislocations; b) Definition of hydride-stress orientation angle φ in the basal plane; c1-c2) Interaction between the background stress and hydride and between the background stress and shielding dislocations for hydride orientation angle $\varphi = 0°$; d1-d2) Corresponding interactions for orientation angle $\varphi = 90°$.

a valid assumption that has been previously adopted for the non-irradiated conditions considered here in the sense that both basal and pyramidal slip require considerably higher resolved shear stresses than prismatic slip (Liu et al., 2023; Reali et al., 2021b). However, this is not true for irradiated conditions (Reali et al., 2021b) and detailed studies in three-dimensional (3D) space have considered activity in all three slip system families (Caillard et al., 2018; Taherijam et al., 2023; Szewc et al., 2016); controversy however remains in terms of which family dominates at particular stress-temperature ranges and the overall complexity in slip behaviour increases dramatically once slip transmission through the hydride-matrix interface is considered (Liu et al., 2023). Full account of these effects would require a 3D Discrete Dislocation Dynamics (DDD) model, which would require extensive developments and immense complexity far beyond current capabilities of state-of-the-art approaches (Tummala et al., 2018); such a model development goes beyond the purposes of the present study and will be considered in the future.

Following nucleation, each dislocation i glides with the aim, in principle, to superimpose its stress field $\sigma^i_{ij_s}$ to the background σ_{oij} and hydride misfit σ_{ij_h} fields such that the total stress field:

$$\sigma_{ij} = \sigma_{ij_h} + \sigma_{oij} + \sum_{i=1}^{k} \sigma^i_{ij_s} \tag{2}$$

gives a minimum strain energy in the domain (Zheng et al., 2019). When a dislocation meets an obstacle, it can only escape from it when it experiences a resolved shear stress that exceeds the obstacle strength i.e. $\tau > \tau_{obs}$, the latter defined here as $\tau_{obs} = 3\tau_{s0}$ where $\tau_{s0} = 152$ MPa is the source strength (also CRSS) at room temperature. Eq. (2) assumes an infinite domain without free surfaces or traction boundaries and hence our DDP analysis does not require the solution of a boundary value problem (Van der Giessen and Needleman, 1995), i.e. the dislocation structure at the end of a time increment is solely determined by the superposition of analytical stress fields at the beginning of the increment.

From a physical perspective, the above assumption of an infinite domain enables us to simulate intragranular hydrides—the box in which Frank-Read sources and obstacles exist is surrounded by a larger box of 10 μm square size within which the dislocations can glide but cannot escape; this resembles a grain with impenetrable boundaries which here serve in generating the back stresses necessary for the dislocation structure to equilibrate, as explained in Skamniotis et al. (2024). From a computational perspective, the assumption of an infinite domain and the associated analytical treatment of dislocations through Eq. (2) offer substantial benefits in computational efficiency and computer code accessibility compared to conventional coupled DDP-FE schemes (Zheng et al., 2019; Ayas et al., 2015); this aligns with our intent to develop fast modelling frameworks that can be used in practise to explore the extremely large parameter space.

Our DDP domain is discretised by prismatic slip planes (0°, 60°, 120°) using a plane separation distance of $120b$ μm. The random distribution of sources and obstacles satisfies minimum spacing criteria as defined in Table 1. We postulate that the (111) plane and $[1\bar{1}0]$ direction of the δ-hydride (FCC) are parallel to the (0001) plane and $[11\bar{2}0]$ direction of the Zirconium HCP matrix, respectively. We thus also assume that slip through the hydride occurs in two systems of the family {111} (out of the four systems), which align with the two prism systems of the Zirconium matrix; this is consistent with (Patel et al., 2021; Reali et al., 2022a; Bradbrook et al., 1972). We also assume that the hydride (γ or δ phase) has the same elastic properties as the matrix. Additionally, building on our recent investigation (Skamniotis et al., 2024), we assume that the time scale of the thermomechanical load cycling (min) is much longer than the time scale of time dependent slip phenomena associated with creep deformation, such as the thermally activated escape of dislocations from obstacles (Zheng et al., 2016a; Liu et al., 2022; Zheng et al., 2016b; Zhang and Dunne, 2017). We therefore assume that all phenomena related to plasticity occur in a quasi-static manner, which justifies the adoption of the classical time independent criterion for dislocation unpinning from obstacles (Reali et al., 2022a; Balint et al., 2006; Tarleton et al., 2015), i.e. a dislocation escapes from an obstacle immediately when the obstacle strength is exceeded (Skamniotis et al., 2024).

In order to discretise the fast movement of dislocations we use a sufficiently small time increment $dt = 10$ ps (Reali et al., 2022a; Tarleton et al., 2015) and apply 'time-scaling' (Skamniotis et al., 2024; Shishvan et al., 2017) to reduce the number of increments necessary to simulate the time scale of thermomechanical loading. This includes converting physical time (min) to DDP time (μs), such that the time duration of all phases of the cycles in Fig. 2a (i.e. heating/cooling/stress increase/stress decrease etc.) are scaled down equally to a reference DDP time $t^* = 100\ t_s$, where t_s is the source nucleation time; t^* is long enough to guarantee that time scaling does not influence the results (Skamniotis et al., 2024).

4.2. Interaction strain energies

In our 2D plane strain problem, the total strain energy U per unit depth (J/m) over an area A can be written as:

$$U = U_o + U_h + U_s + U^I_{oh} + U^I_{os} + U^I_{hs} \tag{3}$$

where the subscripts o, h, s denote energies associated with the background stress, the hydride(s) and the dislocations, respectively, whereas the superscript I designates interaction between each of these, such that:

$$U_o = \frac{1}{2}\int_A \boldsymbol{\sigma_o} : \boldsymbol{\varepsilon_o} dA \tag{3a}$$

$$U_h = \sum_{i=1}^{m} U_{h_i} + U^I_{hh} = \frac{1}{2}\sum_{i=1}^{m}\int_A \boldsymbol{\sigma_h^i} : \boldsymbol{\varepsilon_h^i} dA + \frac{1}{2}\sum_{\substack{i=1 \\ i\neq j}}^{m}\sum_{j=1}^{m}\int_A \boldsymbol{\sigma_h^i} : \boldsymbol{\varepsilon_h^j} dA \tag{3b}$$

$$U_s = \sum_{i=1}^{k} U_{s_i} + U^I_{ss} = \frac{1}{2}\sum_{i=1}^{k}\int_A \boldsymbol{\sigma_s^k} : \boldsymbol{\varepsilon_s^k} dA + \frac{1}{2}\sum_{\substack{i=1 \\ i\neq j}}^{k}\sum_{j=1}^{k}\int_A \boldsymbol{\sigma_s^i} : \boldsymbol{\varepsilon_s^j} dA \tag{3c}$$

$$U^I_{oh} = \frac{1}{2}\int_A (\boldsymbol{\sigma_o} : \boldsymbol{\varepsilon_h} + \boldsymbol{\sigma_h} : \boldsymbol{\varepsilon_o}) dA \tag{3d}$$

$$U^I_{os} = \frac{1}{2}\int_A (\boldsymbol{\sigma_o} : \boldsymbol{\varepsilon_s} + \boldsymbol{\sigma_s} : \boldsymbol{\varepsilon_o}) dA \tag{3e}$$

$$U^I_{hs} = \frac{1}{2}\int_A (\boldsymbol{\sigma_h} : \boldsymbol{\varepsilon_s} + \boldsymbol{\sigma_s} : \boldsymbol{\varepsilon_h}) dA \tag{3f}$$

where ':' denotes element-by-element multiplication of stress $\boldsymbol{\sigma}$ and strain $\boldsymbol{\varepsilon} = \boldsymbol{C}^{-1}\boldsymbol{\sigma}$ tensors, where $\boldsymbol{C}^{-1}$ is the plane strain compliance matrix defined fully by the Zr-4 shear modulus μ and Poisson's ratio ν given in Table 1. The energy of hydrides U_h in Eq. (3b) is decomposed into the sum of individual energies U_{h_i} of m non-interacting hydrides and the interaction energy U^I_{hh} between hydrides; for a single hydride $U^I_{hh} = 0$. Similarly, the energy of dislocations U_s in Eq. (3c) is given by the sum of line energies U_{s_i} of k non-interacting and isolated edge dislocations plus their interaction energy U^I_{ss} (Zheng et al., 2019). All integrations in Eqs. (3a)–(3f) are performed numerically using a small enough gride/element size of 10 nm and a large enough integration area A of 5 μm square size, such that the analytical solution $U_{h_i} = \frac{\pi\mu(\widehat{\varepsilon}L)^2}{4(1-\nu)}$ (Eshelby, 1957) for the strain energy (J/m) of an isolated δ hydride of circular shape ($L = w$) is matched within 2 % error and the line energy $U_{s_i} = \frac{\mu b^2}{4\pi(1-\nu)}\ln\frac{r_1}{r_o}$ (J/m) of an isolated edge dislocation ($r_o = 2b$, $r_1 = 2.5$ μm) is matched within 5 % error.

Positive interaction energy occurs when the superposition of interacting stress fields causes an increase in total energy U and it is therefore energetically unfavourable, i.e. the stress fields repel each other and energy must be offered externally to sustain their interaction (Zheng et al., 2019). On the other hand, negative interaction energy occurs when the interacting stress fields attract each other and tend to minimise U (energetically favourable), as in the case of two edge dislocations with opposite sign. In order to describe the type of interactions taking place in our problem, we provide the strain energy density fields (J/m^3) in Fig. 3 for the idealised and particular case whereby the misfit stress field of a γ hydride ($\widehat{\varepsilon}_x = 0.6$ %, $\widehat{\varepsilon}_y = 5.6$ %) is 'perfectly' shielded/relaxed by dislocations. For the demonstration purposes of this paradigm we utilise a low number of $N = 20$ special-purpose misfit dislocations with extra half planes inside the hydride (two families of 20 dislocations in Fig. 3a1) to mimic the misfit stress field, which are cancelled out by an equivalent $N = 20$ special-purpose shielding dislocations that share the same positions but their extra half planes are outside the hydride (Fig. 3a2); these shielding dislocations also represent the case of a γ hydride with equally negative misfit (i.e. $\widehat{\varepsilon}_x = -0.6$ %, $\widehat{\varepsilon}_y = -5.6$ %). Similar to the special-purpose misfit dislocations, also the special purpose shielding dislocations used here are not crystallographic, i.e., they are artificially orientated horizontally and vertically. However, an interesting theoretical consideration is that the Burger's vector of each of these special-purpose shielding dislocations can be chosen equal to the sum of Burger's vectors of two real crystallographic dislocations that are entangled and lie on two symmetrically intersecting glide planes; this means that the shielding effect of real crystallographic dislocations can be qualitatively represented via these idealised special-purpose shielding dislocations for the purposes of the paradigm shown in Fig. 3.

Fig. 3 shows that the strain energy density field of the single hydride (Fig. 3a1) $u_h = \frac{1}{2}\boldsymbol{\sigma_h} : \boldsymbol{\varepsilon_h}$ is positive and equal to the one arising from the shielding dislocations (Fig. 3a1) $u_s = \frac{1}{2}\sum_{i=1}^{k}\boldsymbol{\sigma_s^k} : \boldsymbol{\varepsilon_s^k} + \frac{1}{2}\sum_{\substack{i=1 \\ i\neq j}}^{k}\sum_{j=1}^{k}\boldsymbol{\sigma_s^i} : \boldsymbol{\varepsilon_s^j}$ such that their interaction strain energy density field (Fig. 3a3) $u^I_{hs} = \frac{1}{2}(\boldsymbol{\sigma_h} : \boldsymbol{\varepsilon_s} + \boldsymbol{\sigma_s} : \boldsymbol{\varepsilon_h})$ is negative and two times higher in magnitude (i.e. $u^I_{hs} = -2u_h$) to satisfy $u_h + u_s + u^I_{hs} = 0$. This also implies that the u^I_{oh} field associated with the interaction between background stress σ_o and hydride misfit (Fig. 3c1 or d1) $u^I_{oh} = \frac{1}{2}(\boldsymbol{\sigma_o} : \boldsymbol{\varepsilon_h} + \boldsymbol{\sigma_h} : \boldsymbol{\varepsilon_o})$ is equal and opposite to the u^I_{os} field associated with the interaction between background stress σ_o and shielding dislocations (Fig. 3c2 or d2) $u^I_{os} = \frac{1}{2}(\boldsymbol{\sigma_o} : \boldsymbol{\varepsilon_s} + \boldsymbol{\sigma_s} : \boldsymbol{\varepsilon_o})$ to satisfy $u^I_{oh} + u^I_{os} = 0$.

The above observations have important theoretical implications on hydride orientation effects. In particular, Fig. 3 implies that perfect shielding of hydride misfit stresses theoretically eliminates any orientation effects. For instance, integration of the interaction fields u^I_{oh} of Fig. 3d1–c1 using Eq. (3d) gives an interaction energy $U^I_{oh} < 0$, which is significantly more negative when $\varphi = 90°$ compared to $\varphi = 0°$, implying that $\varphi = 90°$ is a more energetically favourable configuration. However, $\varphi = 90°$ gives an equally higher $U^I_{os} > 0$ interaction energy than $\varphi = 0°$, such that the orientation effect in the background stress interaction energy terms offset and no configuration is more favourable than the other. In practise, perfect shielding is impossible, because sources of dislocations are limited

in their number and locations, and the flexibility of the nucleated dislocation structure to arrange itself towards minimum energy states is also limited in various ways, e.g. dislocations are restricted to the available slip systems, can be pinned by obstacles and boundaries, and restricted by pile-ups and planar dislocation entanglement caused by superposition of stress fields, etc. Nevertheless, the paradigm of Fig. 3 still indicates that plastic relaxation/shielding of hydride misfit stresses generally acts towards reducing the orientation effect induced by the hydride-background stress interaction; this has not been previously discussed/observed in the literature.

4.3. Orientation effects

In order to explore the above indication drawn from Fig. 3 under realistic cases, i.e., in the presence of real dislocations, we now perform full DDP analysis of a single hydride growth-dissolution cycle for varying orientation φ. We use the temperature-stress $T-\sigma_o$ history in Fig. 2a, with the difference that the background stresses is assumed to be constant $\sigma_o = 130$ MPa. Prior to analysing these DDP results we clarify that our considerations are limited to the HCP basal plane. This implies that all hydride configurations analysed here are 'circumferential' since the cladding texture of interest is the one with the c-axis aligned to the radial cladding tube direction (as in Fig. 1a), which is associated to maximum resistance to DHC failure (Murty and Charit, 2006). In this regard, the cases here where the hydride is perpendicular to the background stress σ_o ($\varphi = 90°$) in Fig. 3d1 and d2 do not represent the so-called 'radial' hydrides associated with the re-orientation effect. Fig. 3b illustrates that an individual hydride can practically grow along three possible directions on the basal plane (Han et al., 2019). If we also consider that the HCP crystal can be rotated about its c-axis at any angle φ with respect to σ_o in the cladding tube, we can reasonably argue that any angle φ between the hydride and the σ_o stress is possible and worth studying.

The DDP results are presented as follows: Fig. 4a and b show the history of all strain energies calculated from Eqs. (3a) to (3f) for $\varphi = 45°$, and $\varphi = 90°$; the dislocation structures and slip contours at the instance Pc (full precipitation as γ phase) are compared between $\varphi = 0°, 45°, 90°$ in Fig. 5a–c, whereas Fig. 5d–f shows how these results change at instance P (γ converts fully into δ). For each case we

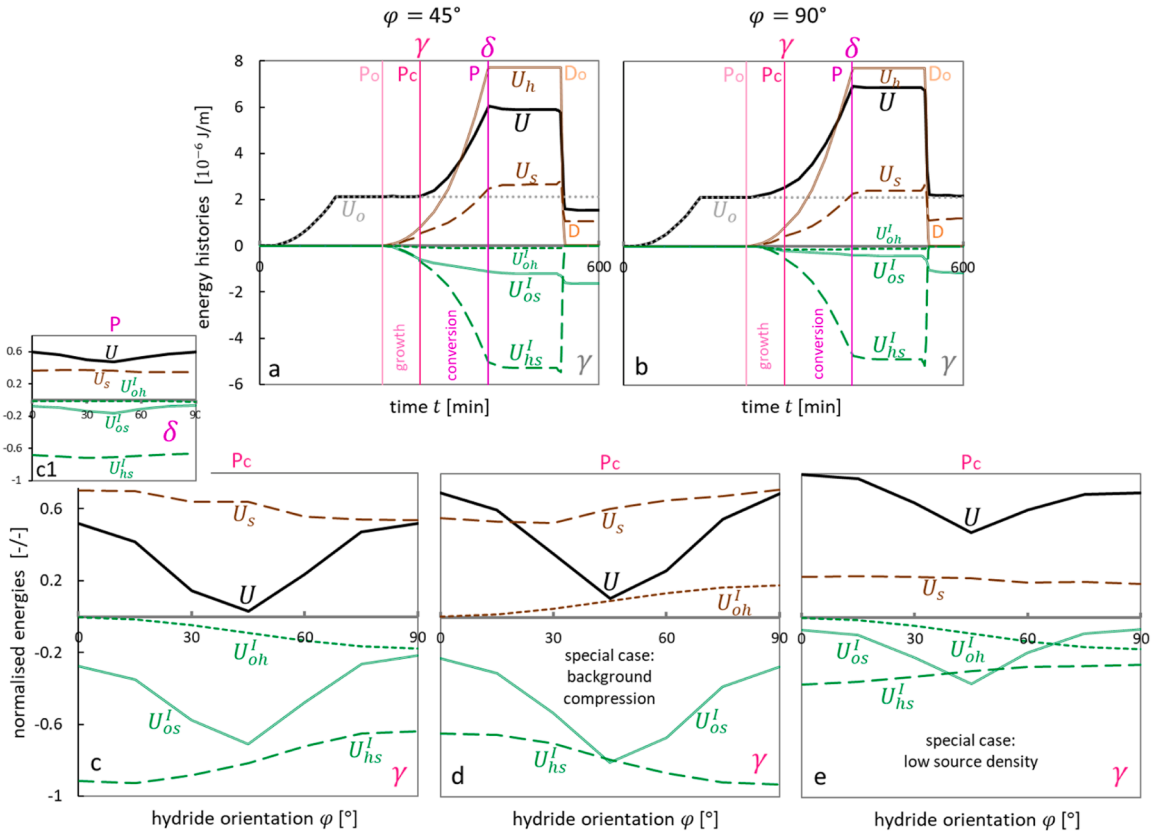

Fig. 4. Strain energy results for the first precipitation of a single hydride. a-b) Time evolution of strain energies defined in Eqs. (3a)–(3f) for two hydride-background stress orientation angles $\varphi = 45°$ and $\varphi = 90°$, under constant background stress $\sigma_o = 130$ MPa; instances Po, Pc, P, Do, D correspond to nucleation, full precipitation as γ phase, full conversion to δ phase, onset of dissolution and full dissolution. c) Strain energies at full γ-precipitation state Pc, normalised by the misfit energy U_h, over the full range of hydride orientation angles φ for—the inset c1) showing the evolution of results on full conversion to δ hydride; d) corresponding results at state Pc for the case of compressive (and constant) background stress $\sigma_o = -130$ MPa; e) corresponding results at state Pc for the case of tensile stress $\sigma_o = 130$ MPa (same as Fig. 4c) with low Frank-Read source density $\rho_{src} = 10\ \mu m^{-2}$ (and slip plane separation $180b$ μm).

also provide the resolved shear stress fields $\tau^i = \tau^i{}_h + \tau^i{}_o$ on the three slip systems i, in the absence of dislocations, normalised by the critical resolved shear stress $\tau_c(T)$ (Fig. 5a1–c1, d1–c1).

It is generally shown that upon conversion from γ hydride to δ, all strain energies (Fig. 4a and b) and dislocation densities increase dramatically for all orientations φ (Fig. 5d–f). This is attributed to the isotropic expansion of δ phase ($\widehat{\varepsilon}_x = \widehat{\varepsilon}_y$) compared to the heavily anisotropic expansion of γ phase ($\widehat{\varepsilon}_y \gg \widehat{\varepsilon}_x$), associated with much higher misfit stresses (Fig. 2b1 and b2) and resolved shear stresses (Fig. 5a1–c1, d1–c1) for δ hydride. As a result, the energy cost of δ hydride misfit $U_h > 0$ dominates in the system, but this is significantly counterbalanced by the $U^I_{hs} < 0$ interaction energy between the misfit and the shielding dislocations (see Fig. 4a and b). However, the equilibrium dislocation structure at the δ hydride state is associated with a strain energy cost $U_s > 0$, which here owes by ~55 % to dislocation-dislocation interactions U^I_{ss} and by the remaining ~45 % to the sum of individual dislocation line energies $\sum_{i=1}^{k} U_{s_i}$. This cost exceeds by far the energy reduction coming from the dislocation interaction with the background stress $U^I_{os} < 0$, let alone the background stress- hydride misfit interaction $U^I_{oh} < 0$, which is negligible for δ in comparison to the other energies involved (see Fig. 4a and b).

All the above result in a positive total energy U cost, which is however reduced significantly by plasticity, e.g. if one removes U_s, U^I_{hs}, U^I_{os} in Fig. 4a this will result in $U = U_o + U_h + U^I_{oh} \approx 10$ x10^{-6} J/m, whereas the current value is 6 x10^{-6} J/m implying a 40 % reduction associated with plasticity. This reduction amount changes with hydride orientation φ since the latter influences dislocation

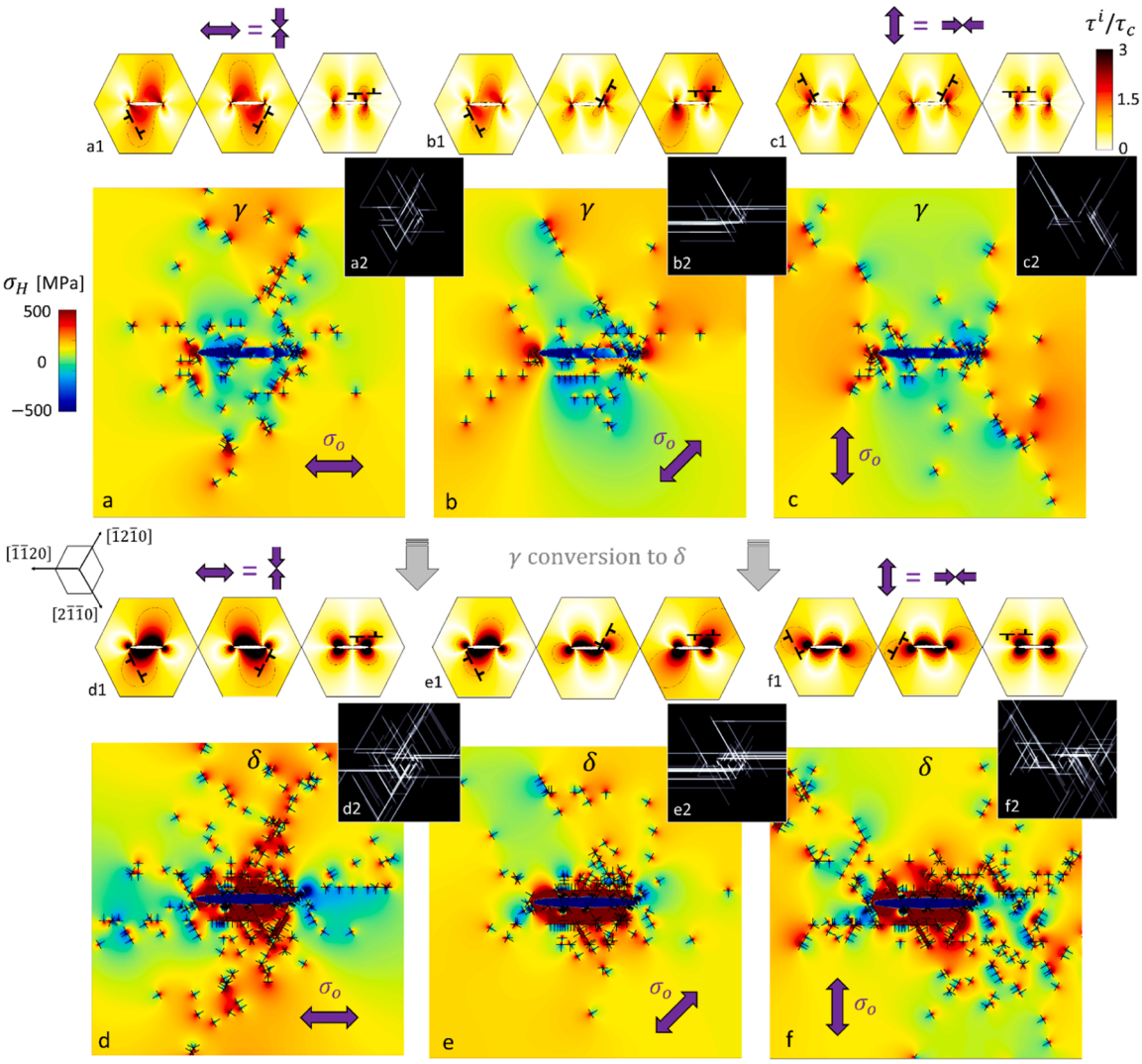

Fig. 5. Hydrostatic stress contours and dislocation structures corresponding to the strain energy histories in Fig. 4a and b. a–c) Results for three hydride orientation angles $\varphi = 0°$, 45°, 90° at state Pc (full precipitation of γ phase). d–f) Corresponding results at state P (full conversion to δ phase). The insets a2–c2 and d2–f2 show plastic slip contours. The insets a1–c1 and d1–f1 show the corresponding resolved shear stress fields in the three slip systems, τ^i normalised by the critical resolved shear stress τ_c, associated with the interaction of hydride misfit and background stress fields (without dislocation fields).

structure. For instance, Fig. 4a and b show that $\varphi = 45^\circ$ enhances the magnitudes of U^I_{hs} and U^I_{os} versus the case of $\varphi = 90^\circ$, leading to a lower U (energetically favourable). The dislocation structures and slip patterns responsible for this effect display strong correlation with the resolved shear stress fields τ^i/τ_c generated by the hydride-background stress interaction. This is more evident in the initial γ phase (Fig. 5a–c) where for each φ case the majority of dislocations and localisation of slip are shown in regions where τ^i/τ_c is high (Fig. 5a1–c1) with slip in the horizontal plane severely enhanced when $\varphi = 45^\circ$ (Fig. 5b2).

Our main finding is that the dependence of U^I_{hs} and U^I_{os} energies on hydride orientation angle φ effectively occurs during the initial growth of the γ phase (instance Pc), rather than the δ. The effect of φ on strain energies is detailed in Fig. 5c for the γ phase and the inset Fig. 5c1 for δ (allenergies are reduced by U_o and then normalised by U_h, since both are invariant with φ); Fig. 5d and e are special cases of γ hydride under compressive background stress and low source density. The dominant effect in all figures is that $\varphi = 45^\circ$ minimises U^I_{os} and this largely determines the minimum total energy U, even when source density is very low ($\rho_{src} = 10\ \mu m^{-2}$—Fig. 5e). The effect weakens substantially upon conversion from γ phase (Fig. 5c) to δ (Fig. 5c1) and one may suggest that any orientation effects prevailing at δ are inherited from its primitive γ phase, which could control initial hydride orientation.

Another key observation is that the $U^I_{oh} < 0$ minimises at $\varphi = 90^\circ$ (Fig. 4c), implying that this would be the energetically favourable orientation in the absence of plasticity; however, in the actual presence of plasticity the effect of U^I_{oh} is counterbalanced by the effect of $U^I_{hs} > 0$ energy which maximises at $\varphi = 90^\circ$ (Fig. 4c). This confirms the previous indications arising from the idealised paradigm of Fig. 3, in that plasticity/shielding acts to cancel out the orientation dependence of misfit strain energy, i.e. the orientation effect induced by the hydride-background stress interaction energy U^I_{oh}. Importantly, we also demonstrate here that the above trends of U^I_{oh} and U^I_{hs} with respect to φ are inverted when a compressive background stress σ_o of equal magnitude is applied (Fig. 5d), which is attributed to the inversion of the resolved shear stress fields, i.e. tensile σ_o along $\varphi = 0^\circ$ gives the same fields as compressive σ_o along $\varphi = 90^\circ$ and vice versa, as indicated in Fig. 5a1–c1.

The central conclusion of Section 4.3 is that while plasticity tends to cancel out orientation effects related to the interaction of hydride misfit-background stress fields, there remains a stronger orientation effect related to the interaction of background stress with the shielding dislocations; this is specific to the γ phase considered here.

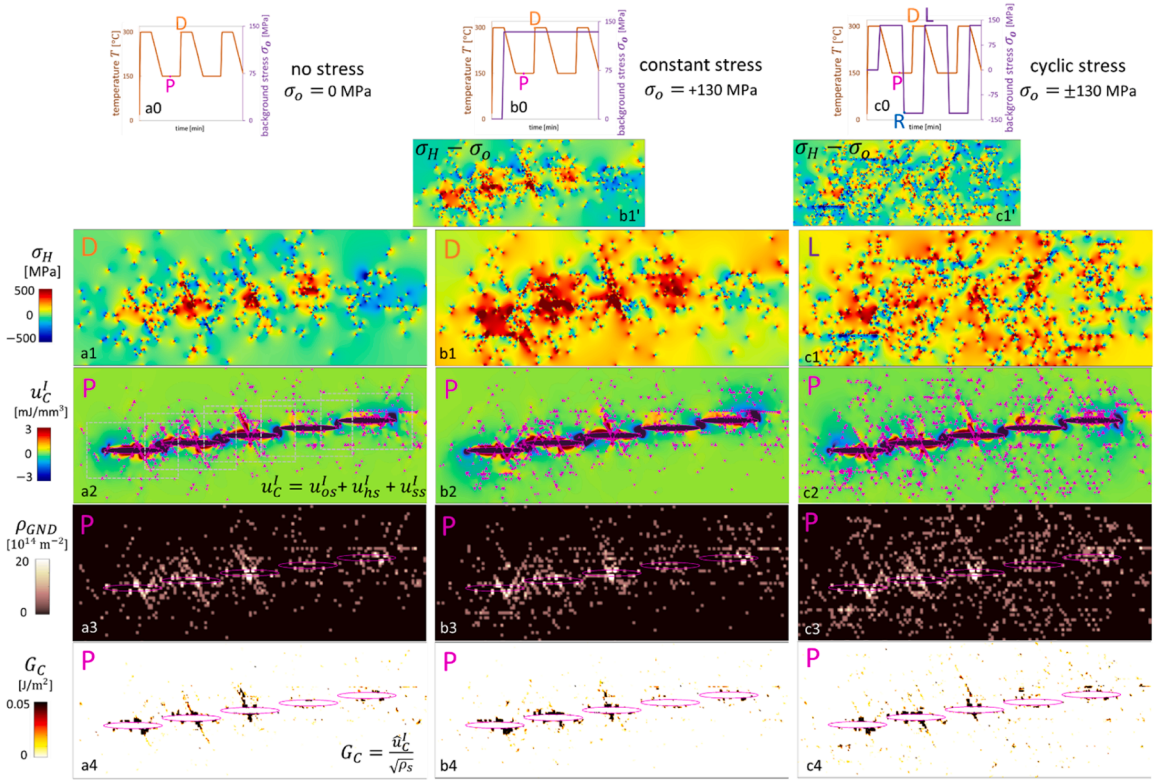

Fig. 6. Qualitative illustration of background stress σ_o history effects at the end of growth of a hydride stringer. a1–c1) Comparison of hydrostatic stress fields σ_H at high temperature dissolution (state D) of four previously precipitated hydrides between the cases of zero stress $\sigma_o = 0$, constant stress $\sigma_o = 130$ MPa and cyclic stress $\sigma_o = \pm 130$ MPa; the insets b1′–c1′ show the corresponding fields of b1–c1 when σ_o is subtracted from the σ_H field. a2–c2) The same comparison is made using the interaction strain energy density field $u^I_C = u^I_{os} + u^I_{hs} + u^I_{ss}$ at the low temperature full precipitation state (P) of the fifth thermomechanical cycle (5 hydrides); the corresponding results at state P of the fifth cycle in terms of the geometrically necessary dislocation density ρ_{GND} and interaction energy area density field G_C are given in Fig. 6a3–c3 and a4–c4.

5. DDP analysis of hydride stringer

We now consider the low energy orientation case $\varphi = 45^\circ$ (identified in Section 4.3) to unravel background stress σ_o history effects during the growth of the hydride stringer shown in Fig. 6. We assume that the stinger in Fig. 6 grows within five consecutive stress-temperature $\sigma_o - T$ cycles, each of them giving rise to a new/child hydride at a predefined location. The centres of hydrides are predefined to be at 1 μm distance from each other and to form an angle of 7° with respect to the horizontal x axis, in line with the previous study by Reali et al. (2022b)—again, we note here that the staircase configuration in Fig. 6 concerns circumferential hydrides in a cladding component and should not be misinterpreted as the configuration of a radial stringer where the hydrides are stacked on parallel basal planes. Comparison is drawn between the three cases of: A) no background stress ($\sigma_o = 0$), B) constant stress $\sigma_o = 130$ MPa and C) cyclic stress $\sigma_o = \pm 130$ MPa (denoted by the $\sigma_o - T$ cycles in Fig. 6a0–c0), and by performing 10 simulations for each case, where each simulation corresponds to a different random distribution of sources and obstacles. The comparison concerns the following results:

a) residual hydrostatic stress field $\sigma_H = \sigma_{xx} + \sigma_{yy}$ (assuming 2D plane stress conditions) at the high temperature dissolution state D (state L for cyclic σ_o) in Fig. 6a1–c1,
b) interaction strain energy density field $u_C^I = u_{os}^I + u_{hs}^I + u_{ss}^I$ associated with dislocations, hydrides and background stress at the low temperature precipitation state P in Fig. 6a2–c2,
c) geometrically necessary dislocation (GND) density field ρ_{GND} at state P in Fig. 6a3–c3,
d) interaction energy area density field G_C at state P in Fig. 6a4–c4.

The σ_H field is used to qualitatively and implicitly indicate the steady state (equilibrium) hydrogen concentration field c^H that prevails after the completion of any transient diffusion process; as explained in Reali et al. (2022a), the c^H and σ_H fields are interrelated through the elastic dipole tensor, such that c^H scales exponentially with σ_H. The u_C^I field is used to indicate the severity of embrittlement and is consistent with the 'configurational' energy density of dislocations (Zheng et al., 2019); as discussed in Reali et al. (2022b); Zheng et al. (2019), regions where a high u_C^I density is stored may be considered as sites for potential crack nucleation—this occurs here at the interfaces between the matrix and the hydrides; the individual energy density fields $u_{os}^I, u_{hs}^I, u_{ss}^I$ included in the u_C^I calculation are plotted in Fig. C1 in Appendix C. In addition to u_C^I, the $\rho_{GND} = \frac{|\sum \boldsymbol{b}|}{bA_s}$ field is also used as a qualitative embrittlement indicator; the sum of the Burgers vectors of all dislocations $|\sum \boldsymbol{b}|$ helps to indicate regions where dislocations are highly aligned, raising the potential for crack initiation; the grid area A_s used for averaging is chosen as $A_s = 0.04 \times 0.04$ μm². Lastly, the $G_C = \frac{\widetilde{u_C^I}}{\sqrt{\rho_s}}$ field is also used here to qualitatively indicate embrittlement and has been proposed in Zheng et al. (2019) as a physically based criterion for crack nucleation; $\widetilde{u}_C^I$ is equivalent to u_C^I with the difference that negative values are ignored (taken as zero), whereas the total dislocation density $\rho_s = N_{dis}/A_s$ (N_{dis} = total number of dislocations) determines the dislocation mean free distance $l_s = \sqrt{\rho_s}$ (and hence an appropriate length scale) over which energy is stored.

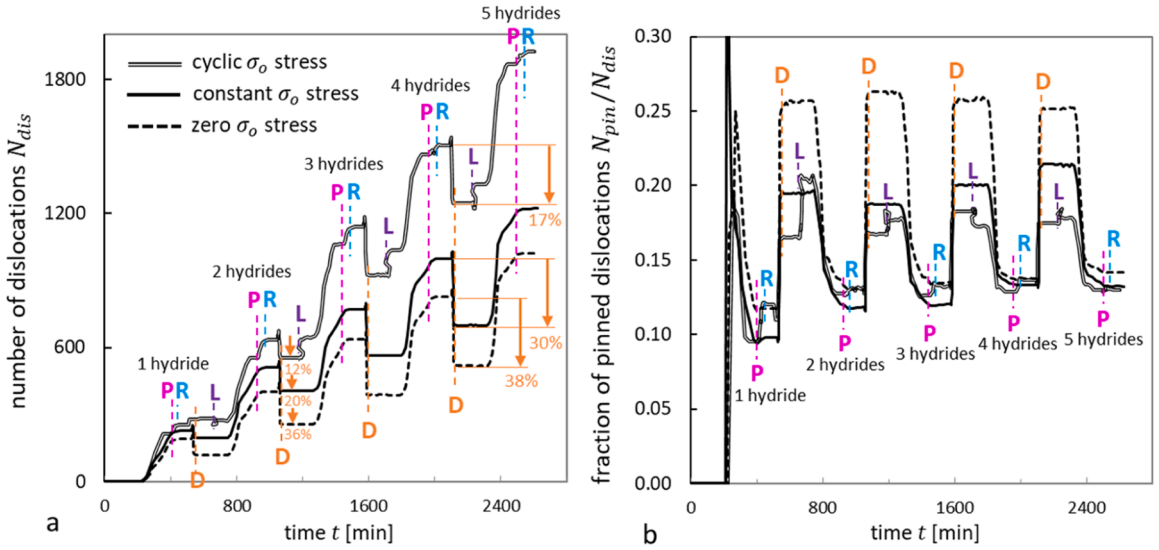

Fig. 7. Quantitative illustration of background stress σ_o history effects during the growth of the hydride stringer in Fig. 6. a) Comparison of the history of total number of dislocations N_{dis} between the cases of zero stress $\sigma_o = 0$, constant stress $\sigma_o = 130$ MPa and cyclic stress $\sigma_o = \pm 130$ MPa. b) Corresponding results in terms of the fraction of dislocations pinned at obstacles N_{pin}/N_{dis}. Results correspond a typical simulation out of the 10 simulations performed for each σ_o case using different source-obstacle distributions.

We firstly present Fig. 6 which shows the outputs of a single typical simulation for each case of background stress history σ_o, corresponding to the same source-obstacle distribution; the following qualitative observations discussed in this paragraph also hold for the other 9 simulations (per σ_o case) corresponding to different random source-obstacle distributions (results now shown). It is shown that the cases of no stress and constant stress σ_o lead to a strong 'memory effect', in the sense that the severe residual tensile hydrostatic stresses σ_H (see Fig. 6a1–b1) are confined to the local regions where hydrides precipitate. Instead, for the case of a cyclic stress σ_o history the severe tensile σ_H values are scattered throughout the domain, and only weakly concentrate at the locations of hydrides (see Fig. 6c1). This difference is attributed to the much larger number of dislocations N_{dis} in the domain for the cyclic stress case compared to the other two cases—this is demonstrated qualitatively by comparison/observation of dislocation structures in Fig. 6a2–c2 and quantitatively by comparison of the N_{dis} histories over the five thermomechanical cycles in Fig. 7a. The intensified dislocation activity in Fig. 6c2 is reflected by the higher ρ_{GND} densities encountered throughout the domain in Fig. 6c3 compared to Fig. 6a3,b3. Nevertheless, the higher number of dislocations for the cyclic stress history does not qualitatively increase the intensity of any of the quantities u_C^I, ρ_{GND}, G_C, locally at the hydride-matrix interfaces (where cracking is expected Reali et al. (2022b)), compared to the other stress histories; the same holds for the maximum values u_C^I, ρ_{GND} and G_C predicted in the domain (results not shown).

We emphasise here that while Figs. 6 and 7 show the results of one simulation corresponding to a single random source-obstacle distribution, the trends discussed above were the same in the other 9 random distributions for which simulations were performed (for each σ_o case); in this regard, we have verified that all the traces in Fig. 7 for the chosen typical simulation represent accurately the key features of the traces that would be obtained by averaging over the 10 simulations; the reason for displaying the traces of one simulation rather than the average traces is because the averaging induces perturbations that are undesirable for the purposes of mechanistic understanding of the traces, as they hinder the interpretation of detailed features, i.e. the small steps in total number of dislocation between dissolution and precipitation; these features will be discussed later in this section. To demonstrate our statistical analysis however we calculate the local average values $\overline{\sigma}_H$, $\overline{u}_C^I$, $\overline{\rho}_{GND}$, $\overline{G}_C$ over the total region enclosed by the five dashed boxes denoted in Fig. 6a2; these calculated spatial averages are then averaged over the 10 simulations. Using this method, we identify two clear trends in terms of the effect of σ_o stress history on the local $\overline{\sigma}_H$ and $\overline{\rho}_{GND}$ averages, which are shown in Fig. 8a and b; the effect of σ_o history on $\overline{u}_C^I$, $\overline{G}_C$ was found to be insignificant and any differences were found to lie within the scatter range (not shown for brevity). Fig. 8a shows that the local average $\overline{\sigma}_H$ is significantly higher for a constant stress history compared to a cyclic stress history, and even further compared to the case of no background stress. These results are consistent with the contours in Fig. 6a1–c1, especially the weakening of the 'memory effect' in the case of cyclic σ_o stress. It is noted, however, that the calculation of the σ_H field (and thus also of $\overline{\sigma}_H$) includes the contribution of background stress σ_o—if we deduct this contribution and instead use the $\overline{\sigma}_H - \sigma_o$ quantity for comparison, we see in Fig. 8a that this quantity is in fact only slightly lower for the case of no stress compared to the constant stresses, which is also qualitatively observed by comparing the $\sigma_H - \sigma_o$ fields between Fig. 6a1 and the inset Fig. 6b1′. This suggests that a constant background stress σ_o does not enhance significantly the 'memory effect' associated with the locally severe residual hydrostatic tensile

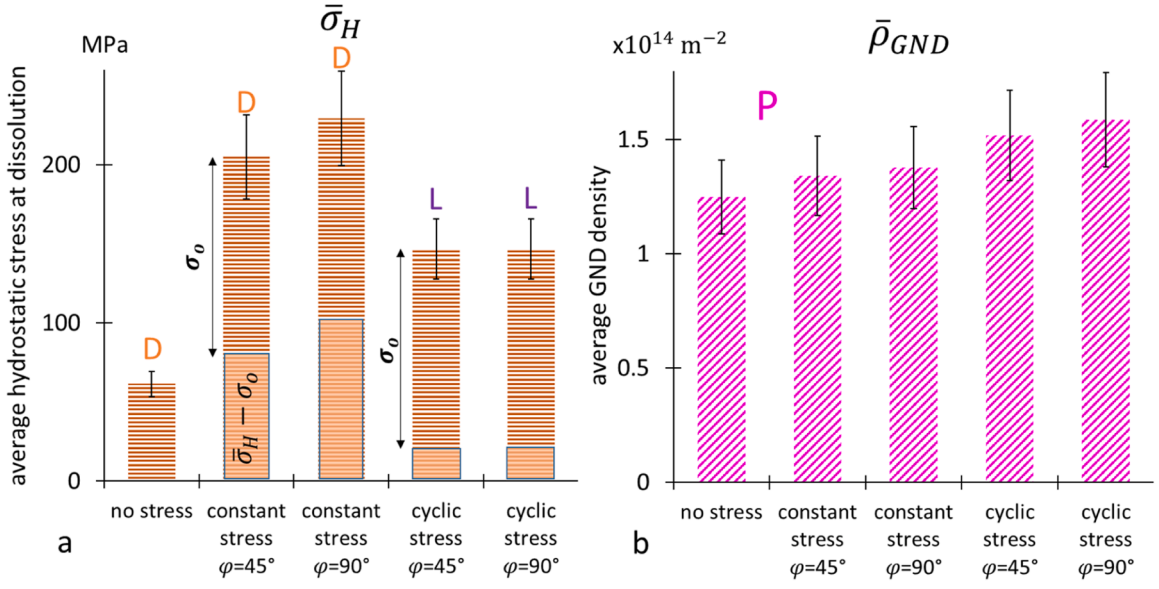

Fig. 8. Quantitative illustration of background stress σ_o history and hydride orientation effects at the end of growth of the hydride stringer in Fig. 6. a) Comparison of residual hydrostatic stress $\overline{\sigma}_H$ at dissolution state D of the fourth cycle, as an average over the local hydride regions denoted by the boxes in Fig. 6a2, between zero stress $\sigma_o = 0$, constant stress $\sigma_o = 130$ MPa and cyclic stress $\sigma_o = \pm 130$ MPa and between two stress-hydride orientation angles $\varphi = 45°$, $\varphi = 90°$ b) Corresponding results at the precipitation P state of the fifth cycle in terms of the geometrically necessary dislocation density $\overline{\rho}_{GND}$ averaged over the same hydride region. The calculations of $\overline{\sigma}_H$ and $\overline{\rho}_{GND}$ take into account only the positive values encountered within the boxed regions of hydrides denoted in Fig. 6a2 (zero or negative values are ignored). We also note that here the results are also averaged over the 10 simulations performed for each σ_o case (in contrast to Fig. 7).

stresses generated at the locations of dissolved hydrides, which implies that the intensified σ_H contours (and implicitly hydrogen concentration) in Fig. 6b1 compared to 6a1 is a consequence of hydrostatic stresses at the grain scale. On the other hand, a cyclic background stress σ_o alleviates drastically the 'memory effect'.

To interpret this weakening memory effect, including the trend in Fig. 8b related to the local average GND density $\overline{\rho}_{GND}$, we firstly consider the evolution of dislocation structure during the first thermomechanical cycle shown in Fig. 9. The case of constant stress σ_o involves two key instances in the cycle: low temperature instance P (Fig. 9a) and high temperature instance D (Fig. 9b), whereas the case of cyclic stress σ_o involves an additional two instances: R (unloading—Fig. 9d) and L (loading—Fig. 9f). In each of these two additional instances, the sign of the background stress σ_o is reverted, causing further slip activity to take place, as shown by the plastic slip contours in Fig. 9d1,f1. Simultaneously, Fig. 7a shows that each of these σ_o reversals (R and L) induces a step increase in the total number of dislocations N_{dis}, i.e., the number of dislocation nucleations exceeds the number of annihilations during the reversal; this feature would not be clear if Fig. 7a displayed the averaged traces over 10 simulations of different source-obstacle distributions. These reversals alone enhance the ratchetting of N_{dis} over the five cycles (Fig. 7a). The ratchetting of N_{dis} is mostly enhanced by the low number of annihilations taking place on each dissolution (instances D), i.e. the high slip irreversibility—Fig. 7a shows a 12 % reduction in N_{dis} at the second dissolution for the case of cyclic σ_o stresses, which almost doubles and triples for the cases of constant σ_o and zero σ_o, respectively; note the same trend qualitatively occurs for the other 9 simulations performed using different source-obstacle distributions. We argue that the increase of slip irreversibility as one goes from the case of no stress to the case of constant stress and then

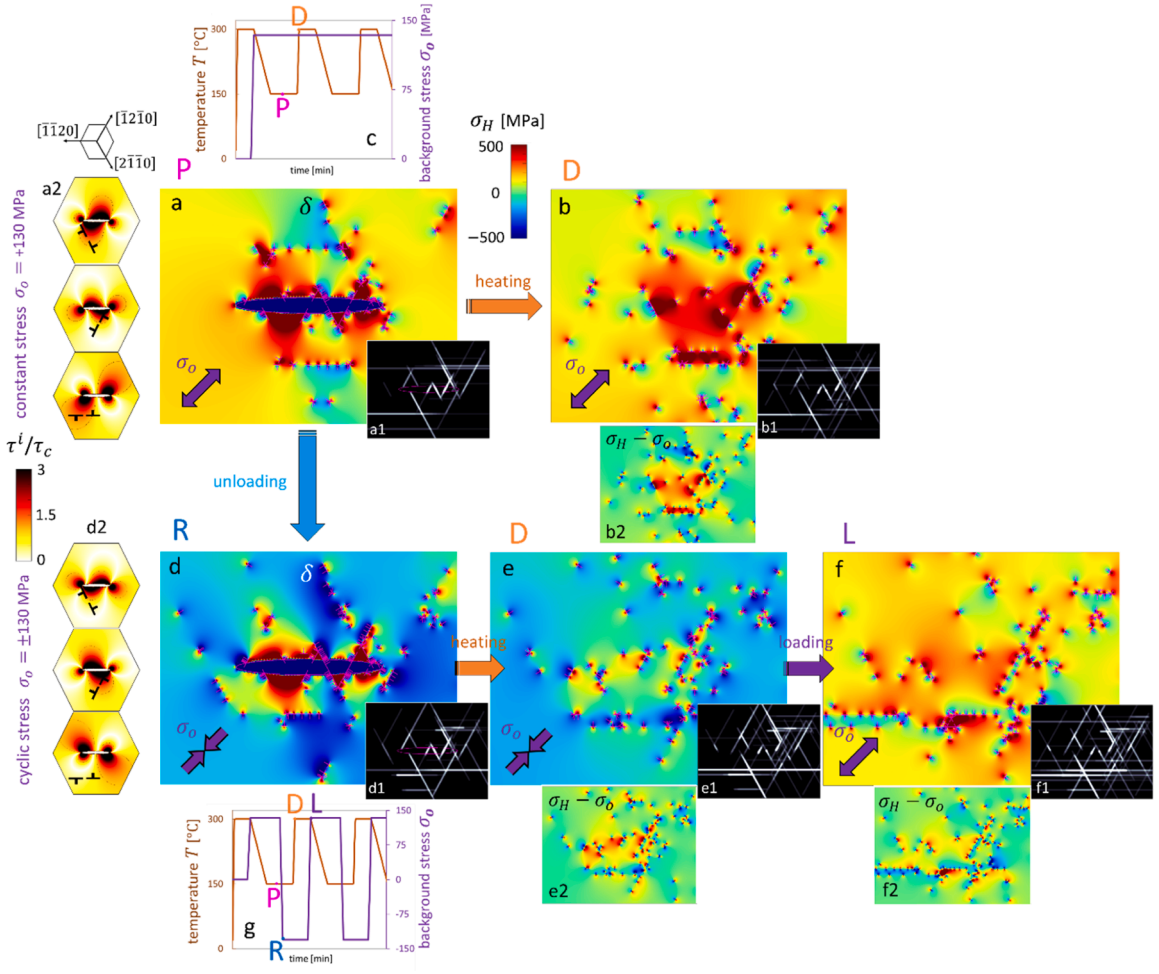

Fig. 9. Qualitative illustration of the effect of background stress σ_o reversals on the dislocation structure and associated hydrostatic stress field σ_H during the first precipitation-dissolution cycle of a single hydride. a-b) Results at two instances in the cycle for the case of constant background stress σ_o = 130 MPa (history in Fig. 9c), including full δ-hydride precipitation state P (a) and full dissolution state D (b). a,d,e,f) Results at four key instances in the cycle for the case of cyclic background stress $\sigma_o = \pm 130$ MPa (history in Fig. 9g), including full δ-hydride precipitation state P (a), full unloading state R (d), full dissolution D at compressive stress (e) and full reloading state L (f). The insets a1,b1,d1,e1,f1 show plastic slip contours; the insets b2, e2,f2 show the residual hydrostatic stress fields if σ_o is subtracted from the calculation of σ_H; the insets a2,d2 show the resolved shear stress fields in the three slip systems, τ^i at states P and R respectively, normalised by the critical resolved shear stress τ_c, associated with the interaction of hydride misfit and background stress fields (without dislocation fields).

to cyclic stress, owes to enhanced dislocation-dislocation interactions rather than enhanced dislocation pinning at obstacles. We base this argument on the trend shown in Fig. 7b where the increase in the fraction of pinned dislocations N_{pin}/N_{dis} during dissolution is maximum for the case of no stress (where slip is most reversible), as compared to the other extreme of cyclic stress for which the increase in N_{pin}/N_{dis} is minimum (where slip is most reversible); since the latter case also corresponds to a much higher N_{dis} than the other two, dislocation-dislocation interactions are believed to contribute more significantly to slip irreversibility than dislocation pinning at obstacles. This argument is also based on the averaging of simulation results out of the 10 different source-obstacle distributions used (not shown).

The weakly localised tensile hydrostatic stresses for the cyclic stress case (Fig. 6c1) is attributed to the growth of a large and irreversible dislocation network over a large zone around the hydrides. The reason why each stress reversal of the cyclic stress history (R and L) enhances this dislocation network partially lies in the following fact: when the background stress σ_o changes sign, it also modifies the resolved shear stress fields τ^i/τ_c related to the hydride-background stress interaction (i.e. without considering dislocations); for example, Fig. 9a2, d2 indicate the differences between these fields between precipitation P (tensile σ_o) and unloading R (compressive σ_o) for the three prismatic slip systems $i = 1,2,3$). It should be noted that the fields in (Fig. 9a2, d2) are specific to the hydride-stress orientation $\varphi = 45^\circ$—if we consider the case $\varphi = 90^\circ$ shown earlier in Fig. 5c1, d1 we can qualitatively appreciate that this involves more severe changes in the τ^i/τ_c fields when the σ_o stress switches from tension (Fig. 5f1) to compression (Fig. 5d1). We therefore argue that the degree by which stress reversals enhance the ratchetting of dislocations N_{dis} depends on the orientation of the hydride with respect to the background stress σ_o, i.e. the angle φ. Indeed, by comparing the N_{dis} history for the case of cyclic σ_o stress in Fig. 7a ($\varphi = 45^\circ$) against the corresponding history for $\varphi = 90^\circ$, we have noticed that the latter orientation results in ~ 15 % higher N_{dis} values (results not shown)—this is consistent with the fact that the τ^i/τ_c fields change more significantly when σ_o switches from tension to compression for $\varphi = 90^\circ$ compared to $\varphi = 45^\circ$. This result is also consistent with the higher local average GND density $\overline{\rho}_{GND}$ shown in Fig. 9b for the case of $\varphi = 90^\circ$ compared to $\varphi = 45^\circ$, although the differences are small and lie within the statistical scatter; this suggests that $\overline{\rho}_{GND}$ is mainly increased by the cycling of background stress rather than the hydride-background stress orientation.

6. Conclusions

We studied the evolution of stresses, strain energies and dislocations underpinning the growth of hydrides associated with the DHC failure mechanism in nuclear Zircaloy components.

Our CPFE analysis at the grain length scale (μm) indicates that tensile plastic deformation at the notch of a cladding component during service/loading can lead to severe compressive residual stresses on service shutdown/unloading. DDP analysis at the hydride scale (nm) can account for such scenarios by modelling hydride precipitation-dissolution under a background stress that cycles between tension and compression to resemble the stress state history at the notch. In this regard, the background stress provides a link between the grain and the hydride length scales.

In the hydride scale, we show that the dislocations that relax the misfit stresses of hydrides can contribute significantly to the total strain energy of the system. Our 2D analysis indicates that the interaction between the stress field of dislocations and the background stress can dominate over the interaction between the hydride misfit stress field and the background stress in reducing the total strain energy of a γ hydride. Although this effect weakens when the metastable γ phase converts to the stable δ phase, this finding generally suggests that dislocations can play a key role in the changes of Gibb's free energy that control microstructural evolution.

The cyclic nature of a background stress is not shown to significantly impact quantities associated with local embrittlement and cracking mechanisms at the hydride-matrix interface (Reali et al., 2022b). This stems from the small differences in configurational energy density of dislocations and density of geometrically necessary dislocations predicted locally at the hydride zones between the cases of zero background stress, constant background stress and cyclic background stress.

On the other hand, a cyclic background stress is shown to drastically modify the distribution of residual tensile hydrostatic stresses generated when hydrides dissolve at high temperature. We find that each background stress reversal enhances slip activity and accelerates the growth of largely irreversible dislocation networks around the hydrides—these networks are such that the tensile residual hydrostatic stresses do not concentrate at the locations of dissolved hydrides, as seen in the cases of constant or zero background stress.

Since the residual tensile hydrostatic stresses are responsible for the accumulation of hydrogen, our findings suggest that depending upon the sequencing between temperature cycling and background stress cycling, as well as the degree of stress asymmetry between compression and tension, the so-called 'memory effect' can be manifested in very different ways. This raises an important question as to whether the details of cladding stress history, along with the temperature history, influence the rate of auto-catalytic hydride nucleation and macro-hydride growth.

Even though we only considered predefined hydride growth histories here without explicitly accounting for the evolution of hydrogen concentration, our study highlights unexplored aspects that are relevant to a broad range of Zirconium hydride modelling frameworks. Our interaction strain energy calculations will guide the future development of thermodynamically consistent discrete dislocation-based models in 2D and/or 3D space, through the coupling of dislocation energies with hydride phase energies and hydrogen diffusion. Simultaneously, our model provides a platform for embedding irradiation effects in the understanding of the DHC process, to aid the design and manufacturing of nuclear alloys.

CRediT authorship contribution statement

Christos Skamniotis: Writing – original draft, Validation, Software, Methodology, Investigation, Formal analysis,

Conceptualization. **Daniel Long:** Visualization, Validation, Software, Formal analysis, Data curation. **Mark Wenman:** Visualization, Supervision, Conceptualization. **Daniel S. Balint:** Writing – review & editing, Visualization, Supervision, Project administration, Funding acquisition, Conceptualization.

Declaration of competing interest

The authors declare the following financial interests/personal relationships which may be considered as potential competing interests:

Daniel Balint reports financial support was provided by Rolls-Royce plc. If there are other authors, they declare that they have no known competing financial interests or personal relationships that could have appeared to influence the work reported in this paper.

Acknowledgements

Rolls Royce is acknowledged for funding this research. Funding was also provided through the EPSRC MIDAS grant EP/S01702X/1. Dr Yang Liu is also acknowledged for the useful discussions and insights throughout the study.

Appendix A. – Details of CPFE analysis

The CPFE method is implemented in the commercial FE Abaqus software. The material constitutive law in Eq. 1 is enforced through the Abaqus user material (UMAT) subroutine. Using a multiplicative decomposition of the deformation gradient $\boldsymbol{F} = \boldsymbol{F}^{\mathrm{e}}\boldsymbol{F}^{\mathrm{p}}$ ($\boldsymbol{F}^{\mathrm{e}}$, $\boldsymbol{F}^{\mathrm{p}}$ are the elastic and plastic deformation gradients) and the crystallographic slip rates $\dot{\gamma}^{i}$ in all slip systems determined from Eq 1, the plastic velocity gradient is computed by:

$$\boldsymbol{L}^{\mathrm{p}} = \sum_{i=1}^{M} \left(\dot{\gamma}^{i}\boldsymbol{n}^{i} \otimes \boldsymbol{s}^{i}\right) \tag{A1}$$

where M is the total number of slip systems (M =3 here), and $\boldsymbol{n}^{i}$, $\boldsymbol{s}^{i}$ denote the unit normal and slip direction vectors of each slip system i ($\otimes$ is the Kronecker product of the two). This enables calculation of the plastic deformation gradient $\boldsymbol{L}^{\mathrm{p}} = \dot{\boldsymbol{F}}^{\mathrm{p}}\boldsymbol{F}^{\mathrm{p}-1}$. We deploy the following Taylor hardening model based on the total current dislocation density, consisted of the statistically stored dislocation density ρ_{SSD} (SSDs) and geometrically necessary dislocation density ρ_{GND} (GNDs):

$$\tau_{\mathrm{c}}^{i} = \tau_{\mathrm{c},0}^{i} + \mu b\sqrt{\rho_{\mathrm{SSD}} + \rho_{\mathrm{GND}}} \tag{A2}$$

where $\tau_{\mathrm{c},0}^{i}$ is the initial critical resolved shear stress for each hardening slip system i, μ is the shear modulus. We assume a linear evolution law $\dot{\rho}_{\mathrm{SSD}} = \gamma^{\mathrm{st}}\dot{\tilde{\varepsilon}}_{pl}$, where γ^{st} is a fitting parameter and $\dot{\tilde{\varepsilon}}_{pl}$ is the cumulative plastic strain rate, whereas the evolution of ρ_{GND} is predicted based on the curl of the plastic deformation gradient (explained by Busso et al., 2000 and by Xu et al., 2021).

Appendix B. – Justification of the assumption of homogeneous inclusion

As discussed thoroughly in the recent study by Liu et al., 2023, the degree of mismatch between the mechanical properties of Zircaloys and their hydrides remains an active research question, underpinned by experimental and modelling challenges. For instance, although the general consensus is that the Young's modulus E between pure Zirconium and hydrides (in the isotropic basal plane) does not differ more than a maximum of ~35% Khan et al., 2021, Reali et al., 2022a, Chan et al., 2016, Zhu et al., 2010, Puls et al., 2005, there exists considerable controversy in the literature with regards to the actual difference. Micro-scale experiments in Chan et al., 2016 measured an E value for δ- hydrides that is only 5% lower than α-Zr, whereas first principles calculations in Zhu et al., 2018 determined a 25% larger value for δ- hydrides and 13% larger for γ-hydrides. Simultaneously, other experiments in Puls et al., 2005 have shown that the properties between Zr and the hydride phase are almost the same for hydrogen compositions up to $ZrH_{1.6}$. As Liu et al pointed out in Liu et al., 2023, the large uncertainty that remains around the degree in which hydride properties change with respect to the ones of the Zircaloy matrix owes to the dependence of these properties upon the original material chemistry, the hydrogen content, as well as the hydrogeneration method. Without doubt, the dynamically changing local hydrogen content of hydrides and the associated transition from one hydride phase to another (e.g. γ into δ here) that occurs in practise, present significant unknowns which are still very hard to quantify Motta et al., 2019.

Given the reportedly small difference between hydride-matrix elastic properties and the large uncertainty around their exact difference, especially for the varying conditions considered in this study, i.e., hydride phase change, temperature variation, increasing hydrogen content with subsequent cycling, we reasonably adopt here the assumption of a homogeneous inclusion, i.e. same properties between hydride-matrix, following the logic described by Reali et al.

As explained by Reali et al., 2022a, this idealisation not only has physical grounds, but also serves to alleviate from the immense computational burden that is added when DDP analysis must account for an elastically inhomogeneous domain. The accurate treatment of elastic inhomogeneity necessitates the solution of a boundary value problem and hence the assumption of a finite domain for the Zircaloy matrix, in contrast to the more favourable assumption of an infinite domain considered in this work, that is well suited to

Zr-hydrides Skamniotis et al., 2024. The authors have analysed inhomogeneous domains through DDP analysis Waheed et al., 2019 based on the method developed by O'day and Curtin, 2004 whereby each homogeneous material region must be solved through a separate DDP sub-problem followed by obtaining a complete solution via superimposition of the individual DDP subproblems with a global Finite Element (FE) solution to satisfy boundary conditions. However, this method has been implemented by a completely different code architecture with the one utilised here; as a result, addressing this code/method incompatibility to eventually model an inhomogeneous inclusion requires a completely new study that must involve substantial and systematic code/method development and verification, since the underlying method by O'Day and Curtin has not been used for inclusion growth-dissolution problems.

All the above indicate that modelling an inhomogeneous inclusion here would have a huge impact on the complexity of the method used with only minimal gain, i.e. while the quantitative results could change depending on the choice of elastic property mismatch (which is currently unknown and largely variable), the qualitative/mechanistic behaviour, the new phenomena unravelled here as well as the messages/conclusions of this study would not be affected. To provide further justification of the anticipated small impact of elastic inhomogeneity on our present study, we present the FE results in Fig. B1 – these show that:

A) the uniform compressive misfit X-stress (i.e. along X-direction) inside a δ-hydride as well as the compressive X-stress at the hydride tip increase by 27% for a inhomogeneous inclusion (Fig. B1a) compared to the homogeneous inclusion (Fig. B1b); the corresponding Y-components of stress are not shown because they are found to differ by a minor amount;
B) X-stresses in the matrix, immediately outside the hydride-matrix interface can increase by 45% (Fig. B1b).
C) when an external traction load of 300 MPa is applied along X axis (Fig. B1c), the stress perturbation caused by the elastic inhomogeneity of the system is negligible compared to the magnitudes of stresses associated with the misfit/transformation strain in Fig. B1b.

However, it should be noted that these results concern the outmost extreme case where the Young's modulus of the inhomogeneous δ-hydride is assumed to be 35% higher than that of the matrix, which is largely unknown. Even for this extreme case of elastic mismatch, the comprehensive pseudo-analytical solutions presented by Khan et al., 2021 indicate that the corresponding increase of misfit strain energy is approximately 25% for the inhomogeneous inclusion (Fig. B1b) compared to the homogeneous (Fig. B1a). This provides reassurance that the trends shown in Fig 4 and the relative significance of dislocation strain energy fields indicated in the present study will remain the same for inhomogeneous hydrides.

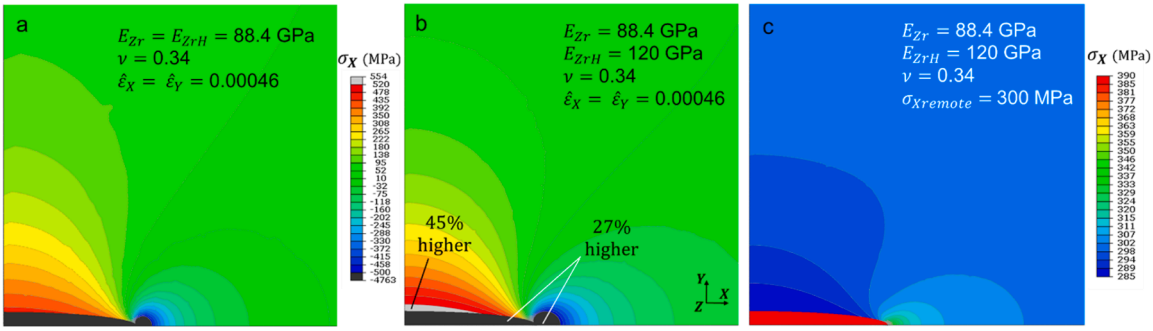

Fig. B1. Stress fields (X-component) of a δ-hydride with elliptical aspect ratio = 10, isolated in an infinite plate, for the following three cases: a) misfit/transformation strain $\hat{\varepsilon}_X = \hat{\varepsilon}_Y$ and homogeneous inclusion, b) misfit/transformation strain $\hat{\varepsilon}_X = \hat{\varepsilon}_Y$ and inhomogeneous inclusion with 35% higher Young's modulus than that of the Zr matrix at room temperature, c) remote traction $\sigma_{Xremote}$ applied along X axis (no misfit/transformation strain) and inhomogeneous inclusion. Solutions are obtained via FE plane stress analysis of a practically infinite plate (10 times larger than hydride) and using symmetry conditions on boundaries. Y-stress components are very similar between cases a) - b) and are insignificant for case c).

Appendix C. – Strain energy density fields for interacting δ-hydrides

Fig. C1 shows strain energy density contours associated with individual interactions between hydrides, background stress and dislocations – these are computed via Eqs 3a-f for state P of the second cycle of the case modelled in Fig 6c2, i.e. two adjacent δ-hydrides. Evidently, the fields u^I_{oh} and u^I_{os} are weak compared to the other fields, suggesting relatively weak interactions between the background stress and the hydrides u^I_{oh} (Fig. C1a) and between the background stress and the shielding dislocations (Fig. C1c). The interaction between the hydrides represented by the u^I_{hh} density field (Fig. C1b) is stronger than the above interactions but results in almost zero total energy U^I_{hh} when integrated over the entire domain. The interactions that dominate in the calculation of $u^I_C = u^I_{os} + u^I_{hs} + u^I_{ss}$ are between the hydride and dislocations i.e. u^I_{hs} in Fig. C1d and between the dislocations themselves, i.e. u^I_{ss} in Fig. C1e; both result in high energy densities stored at the interface between the hydrides and the matrix in Fig. C1f.

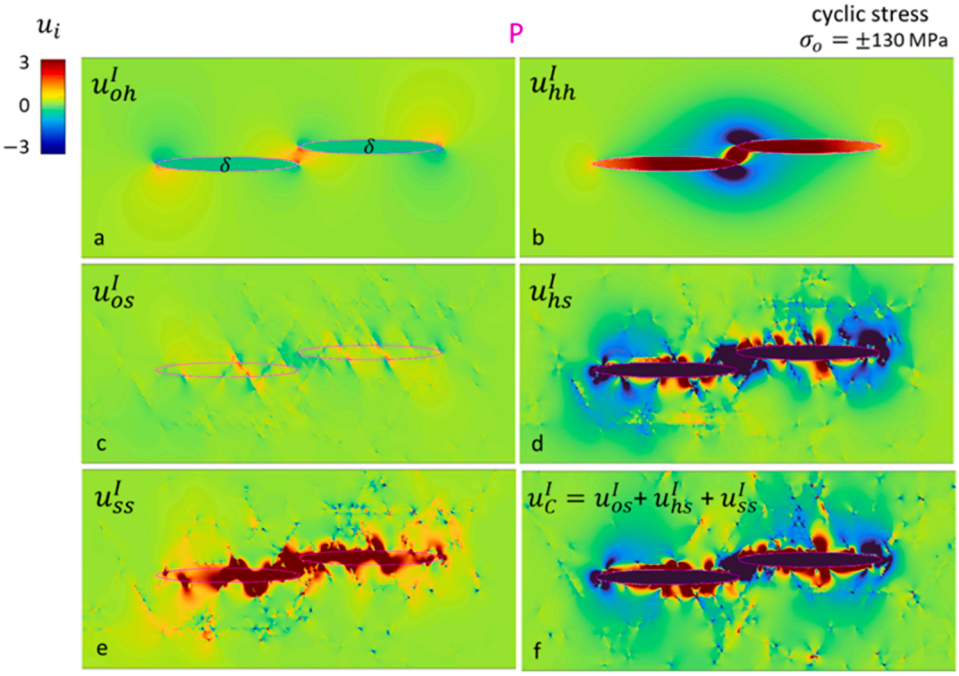

Fig. C1. Interaction strain energy density fields calculated using Eq 3a-f, at the full δ-hydride precipitation state P of the second cycle during the growth of the hydride stringer of case 6c2 (cyclic background stress σ_o).

Data availability

Data will be made available on request.

References

Ayas, C., et al., 2015. Climb-enabled discrete dislocation plasticity analysis of the deformation of a particle reinforced composite. J. Appl. Mech. 82 (7), 071007.
Bair, J., Zaeem, M.A., Schwen, D., 2017. Formation path of δ hydrides in zirconium by multiphase field modeling. Acta Mater. 123, 235–244.
Bair, J., Zaeem, M.A., Tonks, M., 2015. A review on hydride precipitation in zirconium alloys. J. Nucl. Mater. 466, 12–20.
Balint, D.S., et al., 2006. Size effects in uniaxial deformation of single and polycrystals: a discrete dislocation plasticity analysis. Model. Simul. Mater. Sci. Eng. 14 (3), 409.
Bradbrook, J., Lorimer, G., Ridley, N., 1972. The precipitation of zirconium hydride in zirconium and zircaloy-2. J. Nucl. Mater. 42 (2), 142–160.
Busso, E., Meissonnier, F., O'dowd, N., 2000. Gradient-dependent deformation of two-phase single crystals. J. Mech. Phys. Solids 48 (11), 2333–2361.
Caillard, D., Gaumé, M., Onimus, F., 2018. Glide and cross-slip of a-dislocations in Zr and Ti. Acta Mater. 155, 23–34.
Carpenter, G., 1973. The dilatational misfit of zirconium hydrides precipitated in zirconium. J. Nucl. Mater. 48 (3), 264–266.
Chan, H., Roberts, S., Gong, J., 2016. Micro-scale fracture experiments on zirconium hydrides and phase boundaries. J. Nucl. Mater. 475, 105–112.
Chu, H., Wu, S., Kuo, R., 2008. Hydride reorientation in Zircaloy-4 cladding. J. Nucl. Mater. 373 (1–3), 319–327.
Cinbiz, M.N., Koss, D.A., Motta, A.T., 2016. The influence of stress state on the reorientation of hydrides in a zirconium alloy. J. Nucl. Mater. 477, 157–164.
Colas, K., et al., 2014. *Mechanisms of hydride reorientation in zircaloy-4 studied* in situ. In: Zirconium in the Nuclear Industry: 17th International Symposium.
Cui, J., et al., 2009. Delayed Hydride Cracking Initiation at Notches in Zr-2.5 Nb alloys, 131. J. Pressure Vessel Technol., p. 041407
Dunne, F., Rugg, D., Walker, A., 2007. Lengthscale-dependent, elastically anisotropic, physically-based hcp crystal plasticity: application to cold-dwell fatigue in Ti alloys. Int. J. Plast. 23 (6), 1061–1083.
Eshelby, J.D., 1957. The determination of the elastic field of an ellipsoidal inclusion, and related problems. Proc. R. Soc. Lond. Ser. A Math. Phys. Sci. 241 (1226), 376–396.
Gill, S.P., Cornforth, M.G., Cocks, A.C., 2001. Modelling microstructure evolution in engineering materials. Int. J. Plast. 17 (4), 669–690.
Gong, J., et al., 2015. ⟨a⟩ Prismatic, ⟨a⟩ basal, and ⟨c + a⟩slip strengths of commercially pure Zr by micro-cantilever tests. Acta Mater. 96, 249–257.
Han, G., et al., 2019. Phase-field modeling of stacking structure formation and transition of δ-hydride precipitates in zirconium. Acta Mater. 165, 528–546.
Khan, I., Cocks, A., Chattopadhyay, J., 2021. A study of hydride precipitation in zirconium. Mech. Mater. 155, 103773.
Liu, Y., et al., 2021. Hydrogen concentration and hydrides in Zircaloy-4 during cyclic thermomechanical loading. Acta Mater. 221, 117368.
Liu, Y., et al., 2023. Exploring the hydride-slip interaction in zirconium alloys. Acta Mater. 261, 119388.
Liu, Y., Wan, W., Dunne, F.P., 2022. Characterisation and modelling of micro-and macroscale creep and strain rate sensitivity in Zircaloy-4. Mater. Sci. Eng. 840, 142981.
Long, D.J., Wan, W., Dunne, F.P., 2023. The influence of microstructure on short fatigue crack growth rates in Zircaloy-4: crystal plasticity modelling and experiment. Int. J. Fatigue 167, 107385.
Motta, A.T., et al., 2019. Hydrogen in zirconium alloys: a review. J. Nucl. Mater. 518, 440–460.
Murty, K.L., Charit, I., 2006. Texture development and anisotropic deformation of zircaloys. Prog. Nucl. Energy 48 (4), 325–359.
O'day, M., Curtin, W.A., 2004. A superposition framework for discrete dislocation plasticity. J. Appl. Mech. 71 (6), 805–815.
Passelaigue, F., et al., 2021. Implementation and validation of the hydride nucleation-growth-dissolution (HNGD) model in BISON. J. Nucl. Mater. 544, 152683.

Patel, M., et al., 2021. A fast efficient multi-scale approach to modelling the development of hydride microstructures in zirconium alloys. Comput. Mater. Sci. 190, 110279.
Puls, M., Shi, S.-Q., Rabier, J., 2005. Experimental studies of mechanical properties of solid zirconium hydrides. J. Nucl. Mater. 336 (1), 73–80.
Reali, L., et al., 2021a. Plastic relaxation and solute segregation to β-Nb second phase particles in Zr-Nb alloys: a discrete dislocation plasticity study. J. Mech. Phys. Solids 156, 104581.
Reali, L., et al., 2021b. Plasticity of zirconium hydrides: a coupled edge and screw discrete dislocation model. J. Mech. Phys. Solids. 147, 104219.
Reali, L., Balint, D.S., Wenman, M.R., 2022a. Dislocation modelling of the plastic relaxation and thermal ratchetting induced by zirconium hydride precipitation. J. Mech. Phys. Solids 167, 104988.
Reali, L., Balint, D.S., Wenman, M.R., 2022b. Discrete dislocation modelling of δ hydrides in Zr: towards an understanding of the importance of interfacial stresses for crack initiation. J. Nucl. Mater. 572, 154091.
Shi, S.-Q., Xiao, Z., 2015. A quantitative phase field model for hydride precipitation in zirconium alloys: part I. Development of quantitative free energy functional. J. Nucl. Mater. 459, 323–329.
Shishvan, S.S., et al., 2017. Discrete dislocation plasticity analysis of the effect of interfacial diffusion on the creep response of Ni single-crystal superalloys. Acta Mater. 135, 188–200.
Simon, P.-C., et al., 2021. Investigation of δ zirconium hydride morphology in a single crystal using quantitative phase field simulations supported by experiments. J. Nucl. Mater. 557, 153303.
Skamniotis, et al., 2024. On the interaction of grain-scale and hydride-scale stresses in hydrogen enriched Zircalloy nuclear cladding via combined discrete dislocation plasticity and crystal plasticity finite element modelling. Mech. Mater. 195, 105033.
Skamniotis, C., Cocks, A.C., 2022a. Ratchetting and creep failure in twin-wall turbine blades experiencing severe thermal and centrifugal loading. J. Appl. Mech. 89 (9), 091005.
Skamniotis, C., Cocks, A.C., 2022b. Analytical shakedown, ratchetting and creep solutions for idealized twin-wall blade components subjected to cyclic thermal and centrifugal loading. Eur. J. Mech. - A/Solids, 104652.
Sunil, S., et al., 2020. Effect of radial hydride on delayed hydride cracking behaviour of Zr-2.5 Nb pressure tube material. J. Nucl. Mater. 542, 152457.
Szewc, W., et al., 2016. Onset of plasticity in zirconium in relation with hydrides precipitation. Acta Mater. 114, 126–135.
Taherijam, M., et al., 2023. On the effects of transformation strain induced by hydride precipitation. Acta Mater. 261, 119356.
Tarleton, E., et al., 2015. A discrete dislocation plasticity study of the micro-cantilever size effect. Acta Mater. 88, 271–282.
Tondro, A., et al., 2022. Modelling the interactions of zirconium hydrides. Mater. Today Commun. 32, 103933.
Tummala, H., Capolungo, L., Tomé, C.N., 2018. Quantifying the stress state in the vicinity of a δ-hydride in α-zirconium. J. Nucl. Mater. 511, 406–416.
Van der Giessen, E., Needleman, A., 1995. Discrete dislocation plasticity: a simple planar model. Model. Simul. Mater. Sci. Eng. 3 (5), 689.
Vizcaino, P., et al., 2014. Effect of crystallite orientation and external stress on hydride precipitation and dissolution in Zr2. 5 % Nb. J. Nucl. Mater. 447 (1–3), 82–93.
Waheed, S., et al., 2019. Microstructural effects on strain rate and dwell sensitivity in dual-phase titanium alloys. Acta Mater. 162, 136–148.
Wan, W., 2020. Microstructurally-Sensitive Short Crack Growth in Zircaloy-4.
Xiao, Z., et al., 2015. A quantitative phase field model for hydride precipitation in zirconium alloys: part II. Modeling of temperature dependent hydride precipitation. J. Nucl. Mater. 459, 330–338.
Xu, Y., Wan, W., Dunne, F.P., 2021. Microstructural fracture mechanics: stored energy density at fatigue cracks. J. Mech. Phys. Solids 146, 104209.
Zhang, Z., Dunne, F.P., 2017. Microstructural heterogeneity in rate-dependent plasticity of multiphase titanium alloys. J. Mech. Phys. Solids 103, 199–220.
Zheng, Z., et al., 2019. The dislocation configurational energy density in discrete dislocation plasticity. J. Mech. Phys. Solids. 129, 39–60.
Zheng, Z., Balint, D.S., Dunne, F.P., 2016a. Discrete dislocation and crystal plasticity analyses of load shedding in polycrystalline titanium alloys. Int. J. Plast. 87, 15–31.
Zheng, Z., Balint, D.S., Dunne, F.P., 2016b. Rate sensitivity in discrete dislocation plasticity in hexagonal close-packed crystals. Acta Mater. 107, 17–26.
Zhu, W., et al., 2010. First-principles study of different polymorphs of crystalline zirconium hydride. J. Phys. Chem. C 114 (50), 22361–22368.
Zhu, X., et al., 2018. Structure and thermodynamic properties of zirconium hydrides by structure search method and first principles calculations. Comput. Mater. Sci. 150, 77–85.